AD-A137 604 SOLAR-BLIND RAMAN LIDAR(U) NAVAL AIR DEVELOPMENT CENTER 1/1
WARMINSTER PA SENSORS AND AVIONICS TECHNOLOGY
DIRECTORATE A SALIK JUN 83 NADC-83122-30

UNCLASSIFIED F/G 17/5 NL

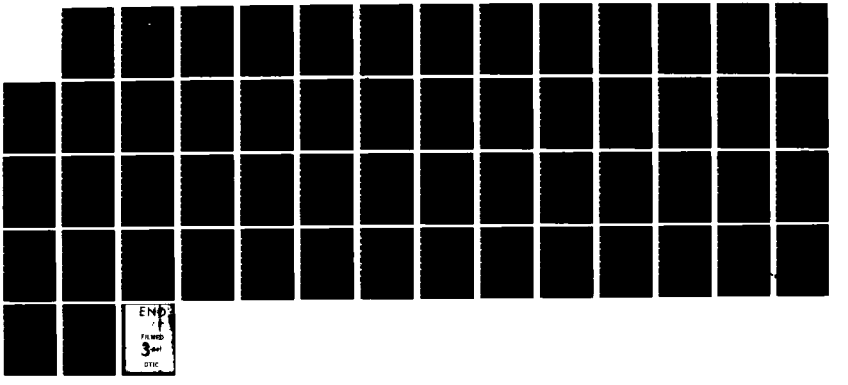

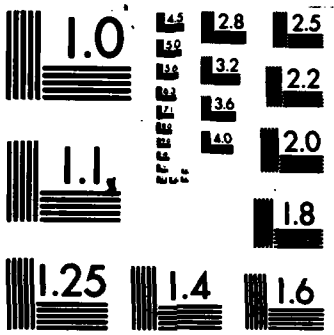

MICROCOPY RESOLUTION TEST CHART
NATIONAL BUREAU OF STANDARDS-1963-A

(12)

REPORT NO. NADC-83122-30

AD A137604

SOLAR-BLIND RAMAN LIDAR PROGRESS REPORT

Alfred Salik
ELECTRO-OPTICS DEVELOPMENT DIVISION
Sensors and Avionics Technology Directorate
NAVAL AIR DEVELOPMENT CENTER
Warminster, PA 18974

JUNE 1983

PHASE II REPORT
AIRTASK NO. A33330H/076B/4WF59-550-000
Work Unit Number JV330

APPROVED FOR PUBLIC RELEASE; DISTRIBUTION UNLIMITED

Prepared For
NAVAL ENVIRONMENTAL PREDICTION RESEARCH FACILITY
Department of the Navy
Monterey, California

NOTICES

REPORT NUMBERING SYSTEM – The numbering of technical project reports issued by the Naval Air Development Center is arranged for specific identification purposes. Each number consists of the Center acronym, the calendar year in which the number was assigned, the sequence number of the report within the specific calendar year, and the official 2-digit correspondence code of the Command Office or the Functional Directorate responsible for the report. For example: Report No. NADC-78015-20 indicates the fifteenth Center report for the year 1978, and prepared by the Systems Directorate. The numerical codes are as follows:

CODE	OFFICE OR DIRECTORATE
00	Commander, Naval Air Development Center
01	Technical Director, Naval Air Development Center
02	Comptroller
10	Directorate Command Projects
20	Systems Directorate
30	Sensors & Avionics Technology Directorate
40	Communication & Navigation Technology Directorate
50	Software Computer Directorate
60	Aircraft & Crew Systems Technology Directorate
70	Planning Assessment Resources
80	Engineering Support Group

PRODUCT ENDORSEMENT – The discussion or instructions concerning commercial products herein do not constitute an endorsement by the Government nor do they convey or imply the license or right to use such products.

APPROVED BY: _____ DATE: 15 Nov 83

UNCLASSIFIED

SECURITY CLASSIFICATION OF THIS PAGE (When Data Entered)

REPORT DOCUMENTATION PAGE		READ INSTRUCTIONS BEFORE COMPLETING FORM
1. REPORT NUMBER NADC-83122-30	2. GOVT ACCESSION NO. AD-A137 604	3. RECIPIENT'S CATALOG NUMBER
4. TITLE (and Subtitle) SOLAR-BLIND RAMAN LIDAR PROGRESS REPORT		5. TYPE OF REPORT & PERIOD COVERED PHASE II REPORT of (SEP 1980 - AUG 1983) 6. PERFORMING ORG. REPORT NUMBER
7. AUTHOR(s) ALFRED SALIK		8. CONTRACT OR GRANT NUMBER(s)
9. PERFORMING ORGANIZATION NAME AND ADDRESS NAVAL AIR DEVELOPMENT CENTER CODE 3012 WARMINSTER, PENNSYLVANIA 18974		10. PROGRAM ELEMENT, PROJECT, TASK AREA & WORK UNIT NUMBERS 62759N, F52553, WK83015, JV330
11. CONTROLLING OFFICE NAME AND ADDRESS NAVAL ENVIRONMENTAL PREDICTION RESEARCH FACILITY MONTEREY, CALIFORNIA 93943		12. REPORT DATE JUNE 1983 13. NUMBER OF PAGES
14. MONITORING AGENCY NAME & ADDRESS(if different from Controlling Office)		15. SECURITY CLASS. (of this report) UNCLASSIFIED 15a. DECLASSIFICATION/DOWNGRADING SCHEDULE

16. DISTRIBUTION STATEMENT (of this Report)

APPROVED FOR PUBLIC RELEASE; DISTRIBUTION UNLIMITED

17. DISTRIBUTION STATEMENT (of the abstract entered in Block 20, if different from Report)

18. SUPPLEMENTARY NOTES

19. KEY WORDS (Continue on reverse side if necessary and identify by block number)

ATMOSPHERIC WATER VAPOR
SOLAR-BLIND
RAMAN LIDAR

20. ABSTRACT (Continue on reverse side if necessary and identify by block number)

PROGRESS OF THE NADC ATMOSPHERIC PROGRAM FUNDED BY THE NAVAL ENVIRONMENTAL PREDICITON FACILITY, MONTEREY, CALIFORNIA, UNDER PROGRAM ELEMENT 62759N, PROJECT F52553 IS REPORTED. LIDAR WATER VAPOR PROFILES ARE PRESENTED ALONG WITH COMPARISON TO LOCALLY ACQUIRED RADIOSONDE DATA.

DD FORM 1 JAN 73 1473 EDITION OF 1 NOV 65 IS OBSOLETE
S/N 0102-LF-014-6601

UNCLASSIFIED

SECURITY CLASSIFICATION OF THIS PAGE (When Data Entered)

TABLE OF CONTENTS

LIST OF ILLUSTRATIONS

INTRODUCTION

This document describes the progress of the NADC Atmospheric Lidar Program funded by the Naval Environmental Prediction Research Facility, Monterey, California, under Program Element 62759N, Project F52553. The objective of this effort is to theoretically determine and experimentally verify the ability of a solar-blind lidar system to remotely measure profiles of atmospheric properties critical to naval operations. The properties chosen for investigation are water vapor concentration, temperature and transmission; with the acquisition of water vapor profiles as the primary goal.

The theoretical feasibility studies have been thoroughly documented via publication in a professional journal[1], a technical report[2] and a text on atmospheric water vapor[3]. In addition, experimental results using a KrF excimer laser were presented at the winter 1983 topical meeting of the Optical Society of America[4]. These results are presented elsewhere in this document.

A major accomplishment of the theoretical feasibility portion of this program was the formulation of a figure of merit (FOM) for water vapor profile acquisition (See Figure 1) and another for temperature[1]. The FOM permits the selection of a best-performance output wavelength for a given set of conditions. This information provides an important design parameter for a solar-blind Raman lidar system, and therefore sets specific requirements on equipment and system performance. The expected changes in optimum operating wavelength as determined by the FOM calculations suggested that the lidar system developed for both water vapor and temperature profile acquisition be tunable.

On the basis of this information, a variable wavelength frequency-doubled dye laser was obtained for use as the lidar transmitter. A major factor in this choice was the production of short, high energy output pulses via a technique known as "cavity dumping". Based primarily on the work of Morton, Mack and Itzkan of Avco Everett Research Laboratories[6], dye laser manufacturers offered this attractive feature as an added option to existing equipment. Unfortunately, the dye laser did not perform as expected, and attempts to acquire water vapor profile in the solar-blind region from 250 nm to 262 nm (both daytime and nighttime) were unsuccessful. A series of experiments aimed at producing acceptable cavity dump performance were undertaken at NADC and independently at Drexel University. None lead to more efficient cavity dumping (See Appendix A). However, nighttime water vapor profiles were acquired using the dye laser system

operating at an output wavelength of 524 nm. These profiles were used to setup the data collection system and software routines and evaluate overall lidar performance. Examples of these results are shown in Figure 2.

At this point, replacement of the dye laser system with a high power fixed-wavelength excimer laser appeared to be the most advantageous solution to the problem. A KrF excimer laser operating at 248.5 nm, with an output energy of ~750 millijoules in a 15 nsec pulse was purchased from Tachisto Incorporated of Needham, Massachusetts and installed as the lidar transmitter. Daytime and nighttime water vapor profiles were acquired in the solar-blind portion of the spectrum using this laser. These profiles and comparison to radiosonde data collected in the same temporal and spatial environment are included in a later section of this document. The replacement of the tunable dye laser system with a fixed-wavelength KrF excimer laser allowed feasibility testing to proceed more rapidly, but it did not provide an appropriate system to evaluate the water vapor FOM. Therefore, the ability of the FOM to quantify the effects of atmospheric ozone on the optimal operating wavelength remains to be experimentally verified. Technologies known to be applicable to tunable KrF excimer systems have developed to where they can be implemented in the existing NADC lidar. Hence, wavelength tunability is seen to be available for implementation as time and funds permit.

Finally, design considerations for the lidar receiver sub-components necessary for the acquisition of atmospheric temperature profiles have been established. A technical memorandum discussing the experimental method and detailing the receiver design is included in Appendix C. To date, June 1983, all major items have been purchased and system modifications necessary to acquire temperature profiles are on schedule.

BACKGROUND

The theoretical details of using a solar-blind Raman lidar to remotely measure atmospheric properties are given in References 1-5. For convenience, a summary of these details follows and a reprint of Reference 1 is included in Appendix B.

The generalized lidar range equation relates the single-scattered laser return signal to physical properties of the lidar and atmospheric parameters as,

$$P(R) = \frac{(ct/2)\ (2T_0)\ P_0 A B \beta(R)}{4\pi R^2} \qquad (1)$$

Where:

$P(R)$ = power returned at range R (watts)

$ct/2$ = range resolution element (meters)

T_o = atmospheric transmission, i.e.
$T_o = e^{-\int_0^R \alpha(R)dr}$

$\alpha(R)$ = atmospheric extinction coefficient

P_o = transmitted power (watts)

A = area of the receiver (meters^2)

B = optical receiver conversion efficiency

$\beta(R)$ = backscatter coefficient (meters^{-1})

The Raman lidar range equation for water vapor profiles relates the ratio of the signal returned from the ν_1 vibrational transition of water vapor molecules to that returned from vibrational transitions of nitrogen molecules, i.e.,

$$P_r(R) = \frac{P_{wv}(R)}{P_{Nit}(R)} = \frac{N_1(R)\ B_1\ \sigma_1\ T_1}{N_2(R)\ B_2\ \sigma_2\ T_2} \qquad (2)$$

Where:

$P_{wv}(R)$ = power returned at the water vapor Raman wavelength (watts)

$P_{Nit}(R)$ = power returned at the nitrogen Raman wavelength (watts)

$P_r(R)$ = ratio of power returned at the Raman wavelengths

$N_1(R)$ = number density of water vapor molecules at range R (meters^{-3})

$N_2(R)$ = number density of nitrogen molecules at range R (meters^{-3})

B_1 = optical conversion efficiency at the water vapor Raman wavelength

B_2 = optical conversion efficiency at the nitrogen Raman wavelength

T_1 = atmospheric transmission at the water vapor Raman wavelength

T_2 = atmospheric transmission at the nitrogen Raman wavelength

σ_1 = water vapor scattering cross-section (m^2)

σ_2 = nitrogen scattering cross-section (m^2)

In the solar-blind Raman lidar system depicted in Figure 2, the optical signals acquired by the photomultipliers are used to extract a profile of the water vapor mixing ratio using,

$$R(R) = \frac{S_1(R) - \bar{N}_1 + K_1}{S_2(R) - \bar{N}_2 + K_2} C \qquad (3)$$

Where:

$R(R)$ = water vapor mixing ratio at range R (gm kgm^{-1})

C = lidar system constant

$S_1(R)$ = signal plus background noise at range R acquired at the water vapor Raman wavelength

$S_2(R)$ = signal plus background noise at range R acquired at the nitrogen Raman wavelength

$\bar{N}_1$ = time averaged background noise at the water vapor Raman wavelength

$\bar{N}_2$ = time averaged background noise at the nitrogen Raman wavelength

K_1 = water vapor channel baseline correction constant

K_2 = nitrogen channel baseline correction constant.

EXPERIMENTAL METHOD

As shown schematically in Figure 3, the Raman return signal receiver is a Cassegrain telescope. The primary mirror (M1) is 30 inches in diameter, the secondary mirror (M2) is 8 inches in diameter and the effective focal length of the system is 296 inches.

The output of the telescope is split into two beams. Each beam is directed via a narrow band optical filter, centered at the appropriate wavelength, into an RCA 310005 solar-blind photomultiplier. Hence, the Raman return signals at 273.3 nm for water vapor and at 263.8 nm for nitrogen are selected and individually amplified. The electrical signal from each photomultiplier is then directed into a Tektronix R7912 fast transient digitizer. The digitized signals are stored on magnetic tapes in a format structured by a Z80 microcomputer system to be compatable with DEC PDP 11/34 Fortran requirements.

To extract a water vapor mixing ratio profile from the raw data, two separate tapes are required. One tape contains the signal plus noise in each of the Raman channels. The other contains information on random, background and systematic noise introduced into the lidar receiver with the laser output beam blocked. This second tape provides baseline information and is necessary for two reasons. First, as noted earlier, the Tektronix R7912 digitizer is a non-zero baseline device. That is, with no signal input to the digitizer, the value of the digital output is a function of the horizontal and vertical trace position and intensity controls. Additionally, each R7912 trace exhibits a slope which depends upon the vertical trace position selected. Secondly, the baseline tape contains information on EMI, RFI and any externally (or internally) generated noise. This bias must be removed from the signal tapes to properly assess the level of the Raman return signal in each channel. To accomplish this goal, the time-average of the baseline tape is used in equation 3 as $\bar{N}_1$ and $\bar{N}_2$. Further, the additive constants K_1 and K_2 compensate for intensity setting induced differences between the data and the baseline tapes.

The range resolution of the lidar system is given by,

$$\Delta R = ct/2 \qquad (4)$$

Where:

ΔR = range resolution (meters)

c = velocity of light (meters sec^{-1})

t = output pulse duration (sec)

The output pulse duration of the lidar transmitter is 15 nsec. Therefore, the lidar range resolution is approximately 2.3 meters. Acquisition of water vapor profiles with this range resolution require the R7912 timebase to be set for 8 micro-

seconds per sweep. This set of factors limits the altitude of the profiles to one-kilometer. This limitation can be circumvented by proper range gating to select any one-kilometer segment of the profile or the maximum range of the lidar can be increased to three kilometers, with a range resolution of approximately 7 meters. Additionally, the range resolution element for any chosen scenario may be increased by averaging the data in adjacent range bins to produce the required resolution. For example, one-kilometer profiles with a range resolution of 2.3 meters can be "range averaged" to produce one-kilometer profiles with a range resolution of 90 meters for comparison to radiosonde data.

Balloon-borne radiosondes were launched from NADC as shown in Figure 4. High resolution lidar water vapor data was acquired immediately prior to, during and following all radiosonde launches. A baseline tape problem precluded the extraction of a water vapor profile from the raw data tapes of the 0600 hours launch on September 28, 1982.

EXPERIMENTAL RESULTS

Lidar range-averaged water vapor profiles and comparison to locally acquired radiosonde data are shown in Figures 5 through 9. Most of the lidar profiles acquired during the episodes listed in Figure 4 were of a routine nature. While all of the lidar profiles compared well to the accompanying radiosonde data, two of the profiles were quite unusual. These profiles exhibit pronounced alternate layers of moist and dry air and are shown in Figures 10 and 11.

These profiles have been the subject of considerable analysis for two reasons. First, the possibility of an instrumental (or external) artifact intruding into the data had to be considered. Extensive examination of the raw data and background noise tapes did not produce convincing evidence of an agency external to the atmosphere as the cause of the structured profiles. In addition, the raw radiosonde humidity ordinate data exhibited very erratic behavior on two of the six launches. The erratic behavior occured during the same approximate altitude as the stratified lidar data and appeared to be operating normally at all other altitudes. The launching of the radiosondes and subsequent analysis of data was performed at NADC by a meterological (MET) team from the Naval Eastern Oceanographic Center (NEOC), Norfolk, Virginia. Discussions with the MET team members provided additional insight into the radiosonde humidity profiles. The erratic behavior of the humidity sensor during the first kilometer had been observed "many times in the past". Since the sensor data is not reliable during these events, the approach

used by the MET team is to "eye-ball integrate" through this region. That is, they perform a linear fit between humidity data points they ascertain to be acceptable. This method produced the smooth radiosonde profiles included on all lidar data presented. The second reason for subjecting the high resolution lidar data to extensive analysis is to provide an understanding of the mechanisms responsible for the stratified appearance of the water vapor profiles. While not part of the present lidar program goal, an understanding of these mechanisms would provide insights which would allow more ambitious future program goals to be considered.

$$\Lambda = \frac{T_o(\lambda_o)\ T_1\ (\lambda_1)\ T_2\ (\lambda_2)}{\lambda_o^4 \quad T_1'\ (\lambda_1)\ T_2'\ (\lambda_2)}$$

Λ = DEFINED FIGURE OF MERIT OF H_2O MEASUREMENT

λ_o = OUTPUT WAVELENGTH

λ_1 = RECEIVED WAVELENGTH, e.g., N_2

λ_2 = RECEIVED WAVELENGTH, e.g., H_2O

$T_o(\lambda_o)$ = ATMOSPHERIC TRANSMISSION TO ALTITUDE (e.g., 1.0 km) AT λ_o

$T_1(\lambda_1)$ = ATMOSPHERIC TRANSMISSION TO ALTITUDE AT λ_1

$T_2(\lambda_2)$ = ATMOSPHERIC TRANSMISSION TO ALTITUDE AT λ_2

$T_1'(\lambda_1)$ = TRANSMISSION THROUGH THE ENTIRE ATMOSPHERE AT λ_1

$T_2'(\lambda_2)$ = TRANSMISSION THROUGH THE ENTIRE ATMOSPHERE AT λ_2

FIGURE 1. FIGURE OF MERIT FOR WATER VAPOR

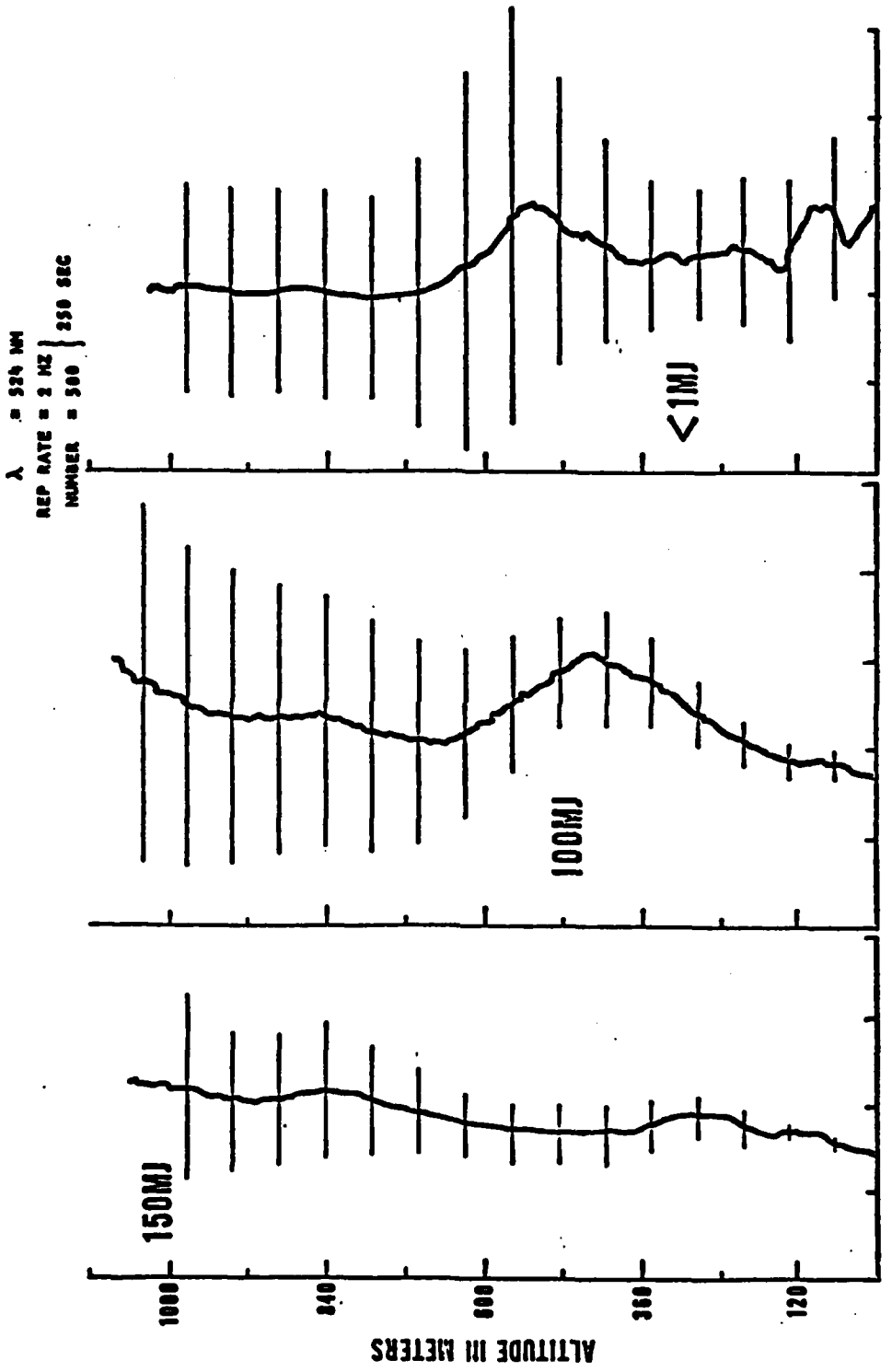

FIGURE 2. DYE LASER WATER VAPOR PROFILES

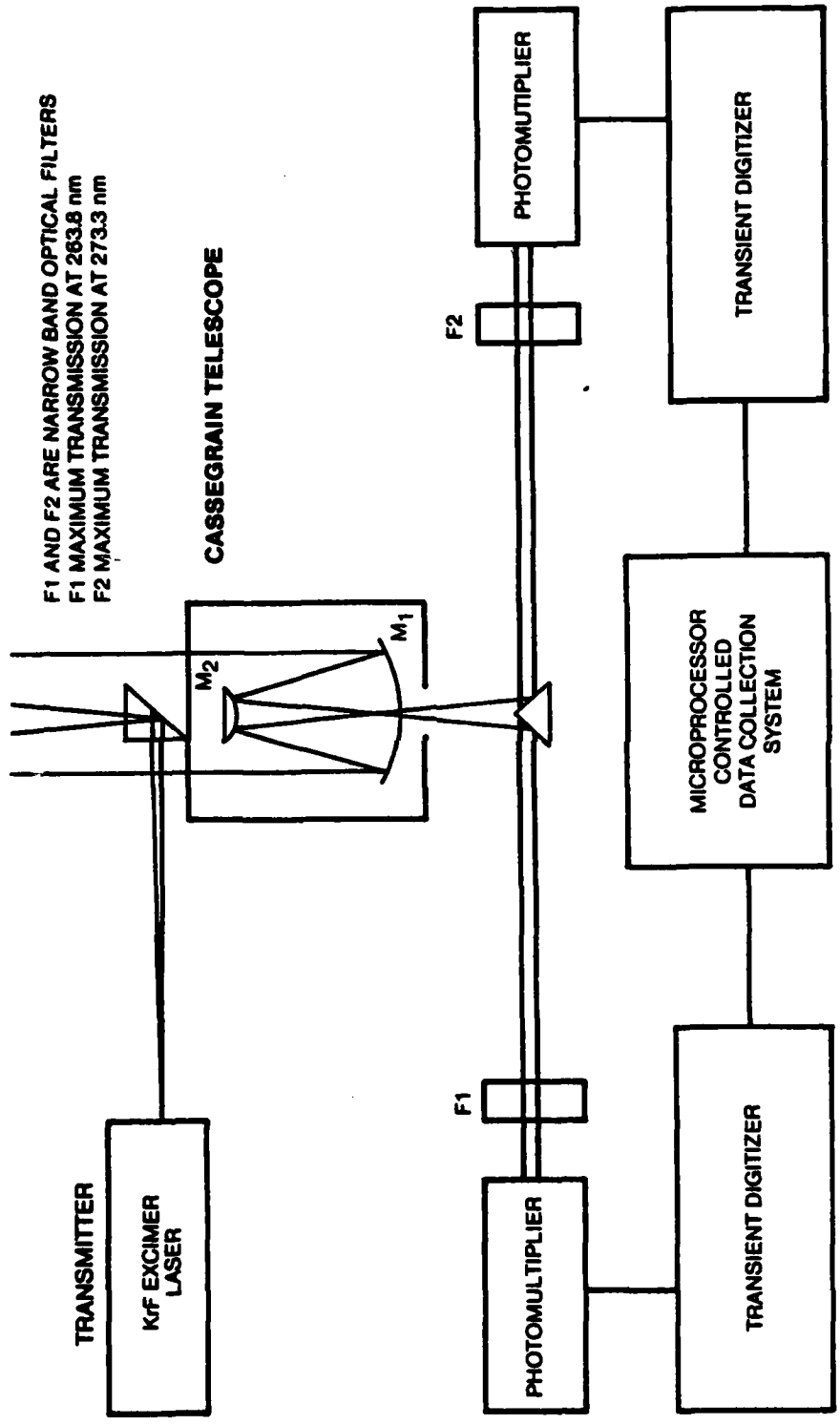

FIGURE 3. SOLAR BLIND LIDAR BLOCK DIAGRAM

DATE (1982)	LAUNCH TIME (EASTERN STANDARD TIME)
SEPTEMBER 27	1800 HOURS
SEPTEMBER 28	0600 HOURS
SEPTEMBER 28	1800 HOURS
SEPTEMBER 29	0600 HOURS
SEPTEMBER 29	1800 HOURS
SEPTEMBER 30	1100 HOURS

FIGURE 4. RADIOSONDE LAUNCHING SCHEDULE

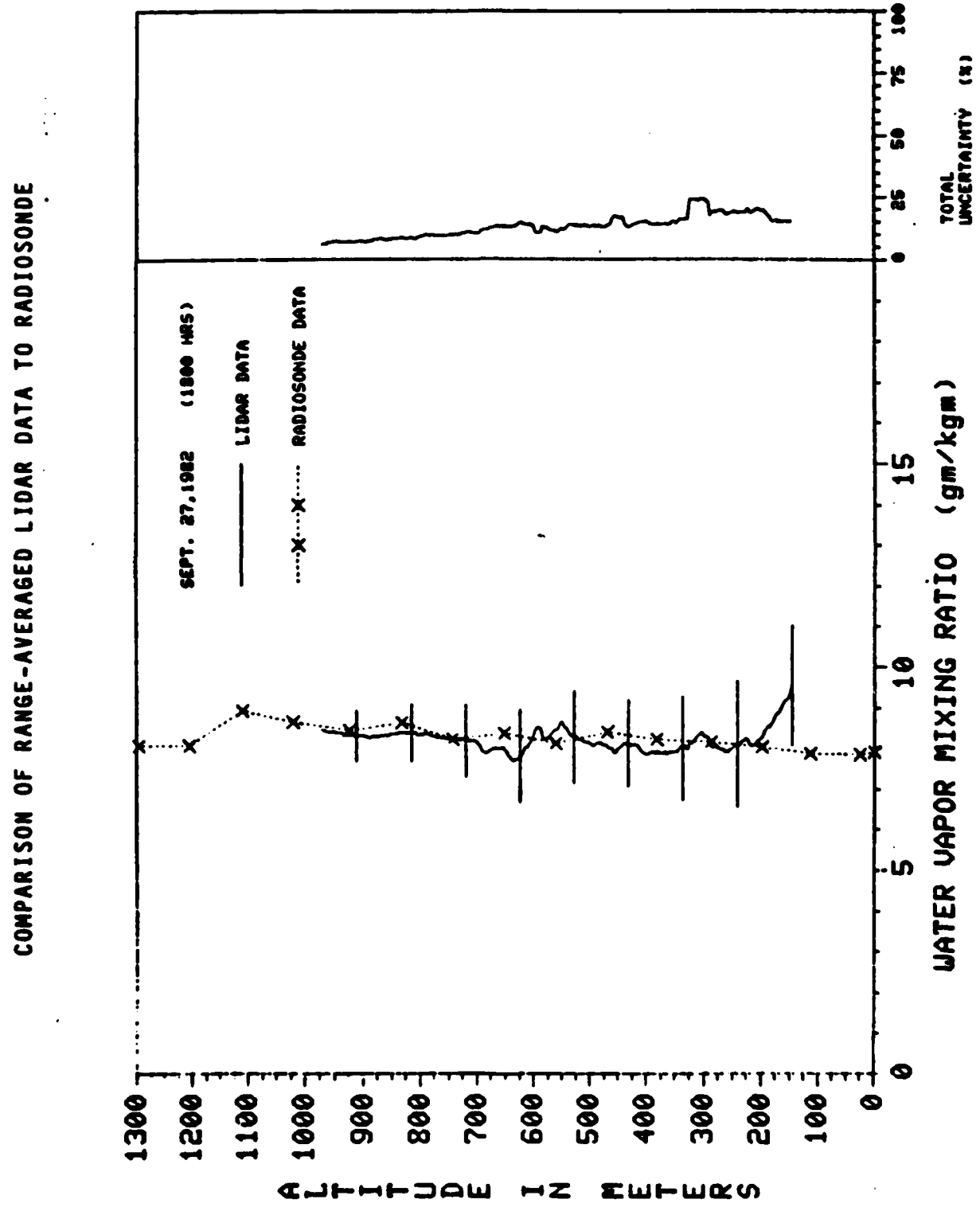

FIGURE 5. LIDAR WATER VAPOR PROFILE

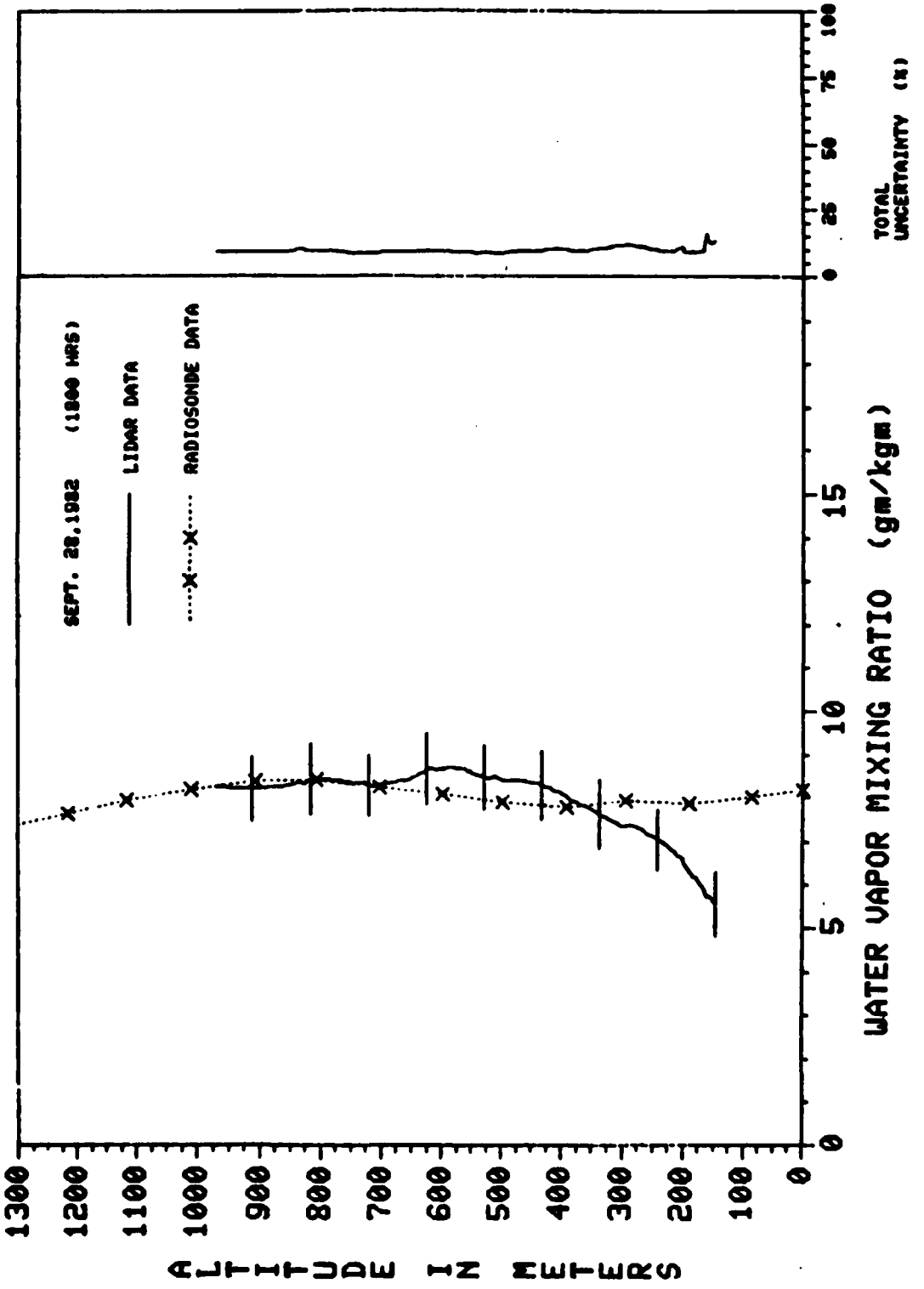

FIGURE 6. LIDAR WATER VAPOR PROFILE

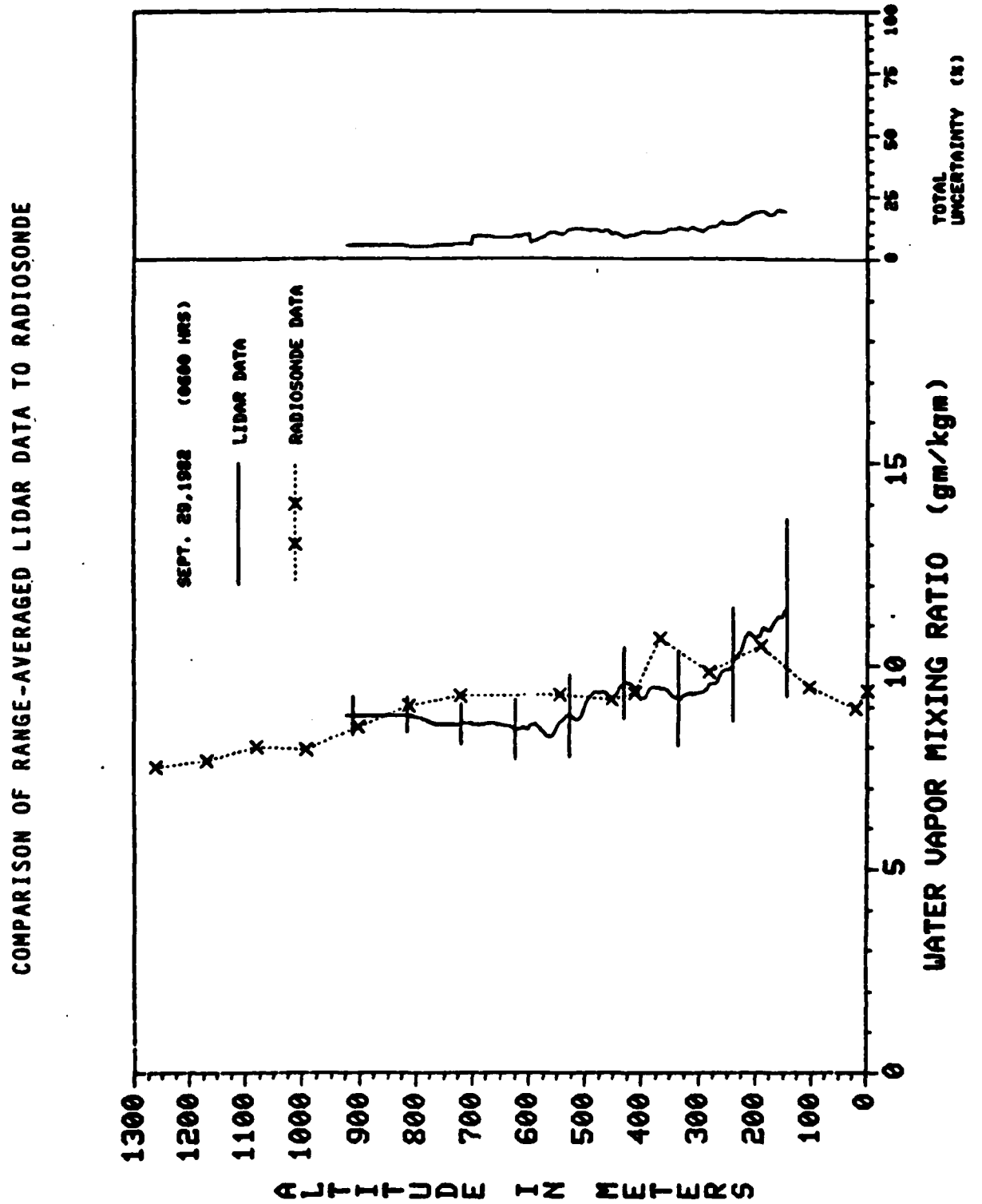

FIGURE 7. LIDAR WATER VAPOR PROFILE

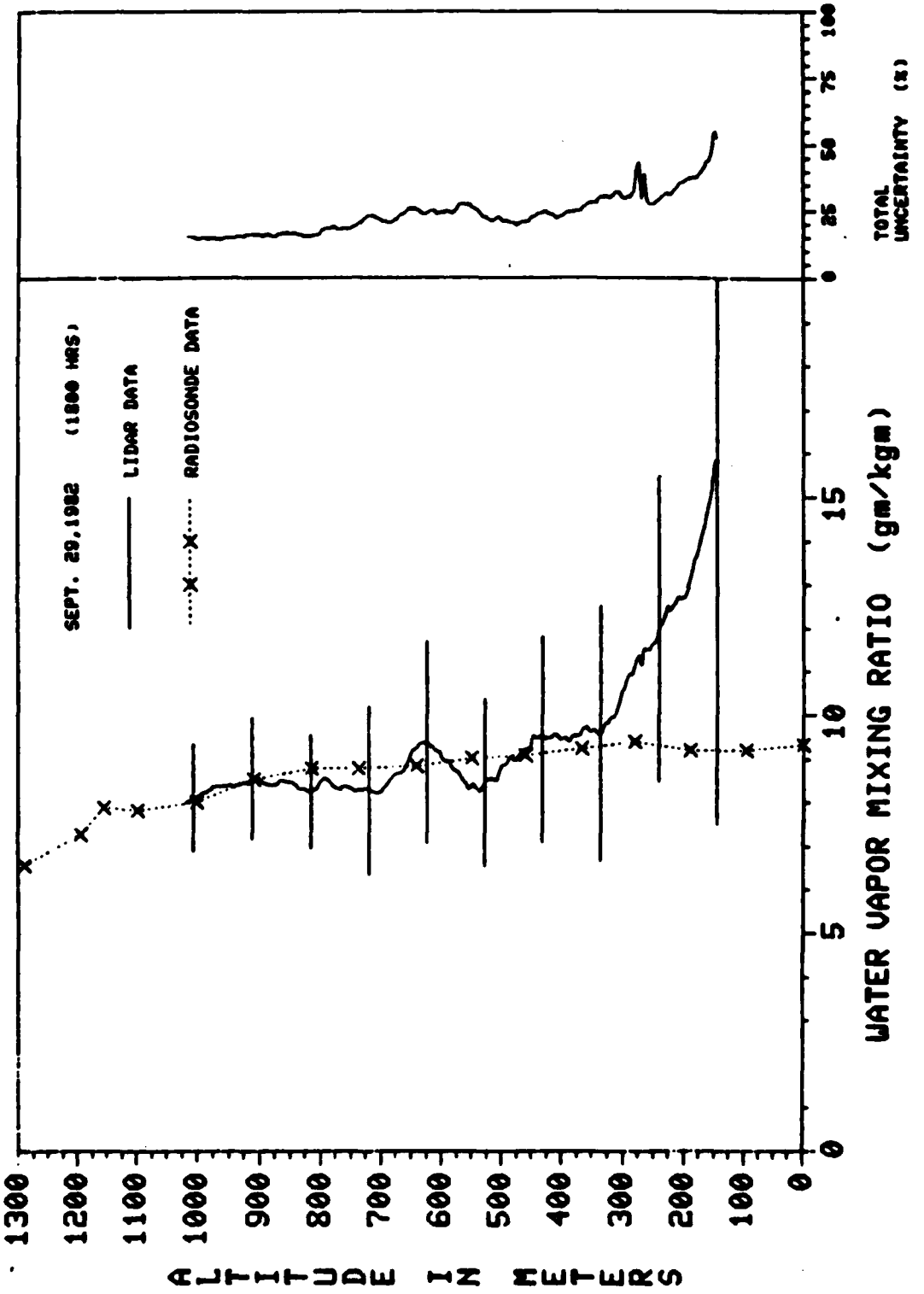

FIGURE 8. LIDAR WATER VAPOR PROFILE

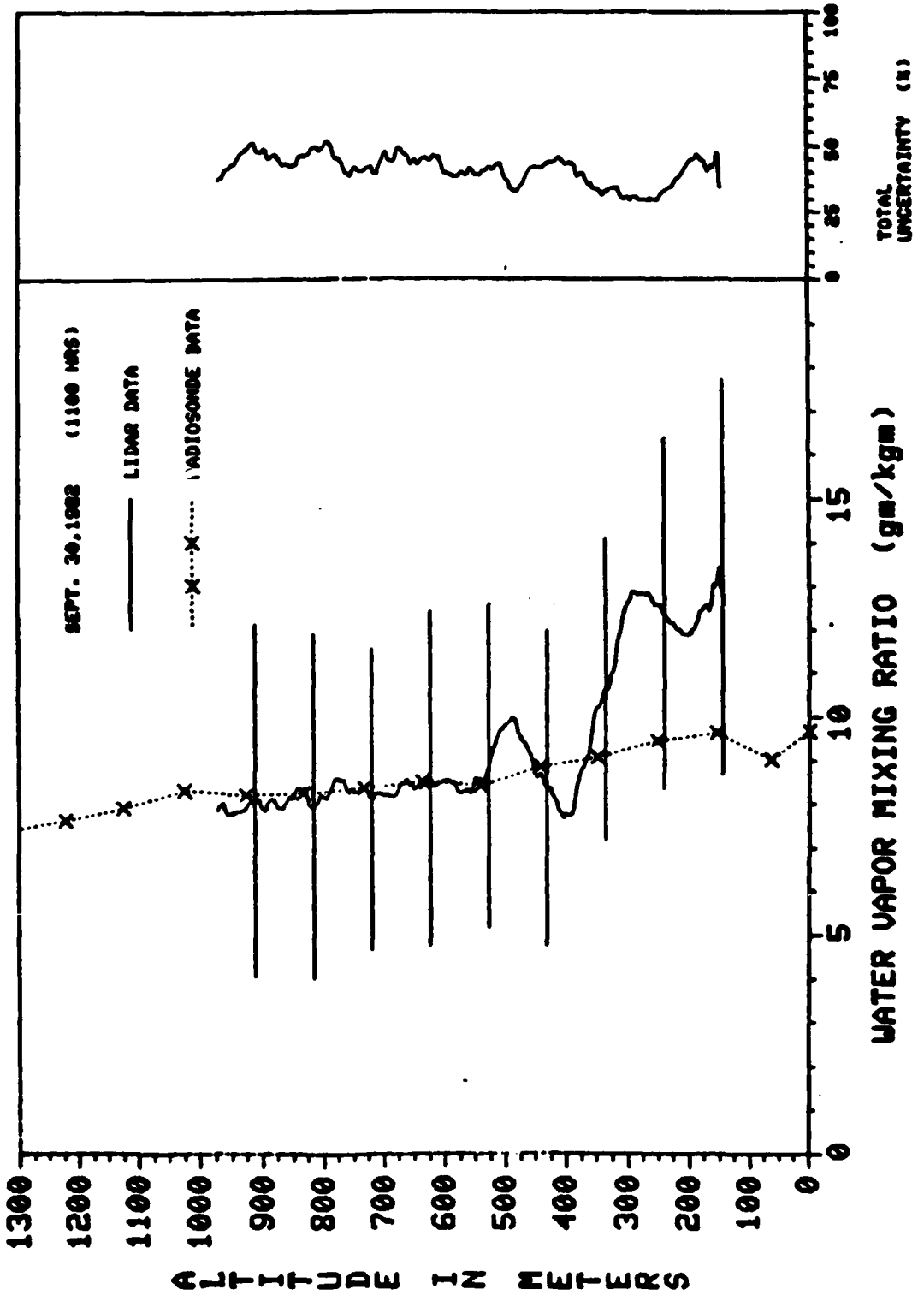

FIGURE 9. LIDAR WATER VAPOR PROFILE

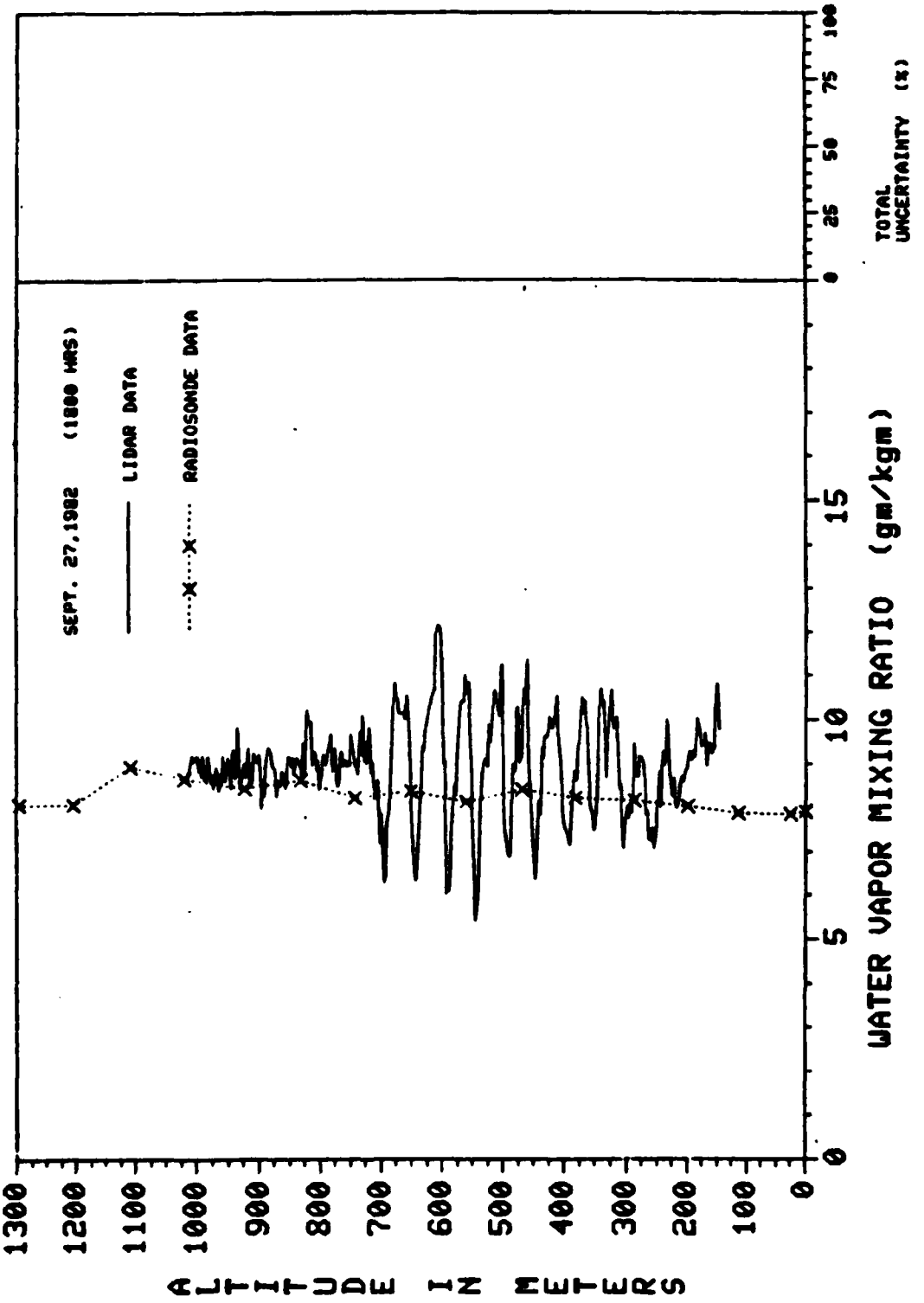

FIGURE 10. HIGH RESOLUTION LIDAR PROFILE

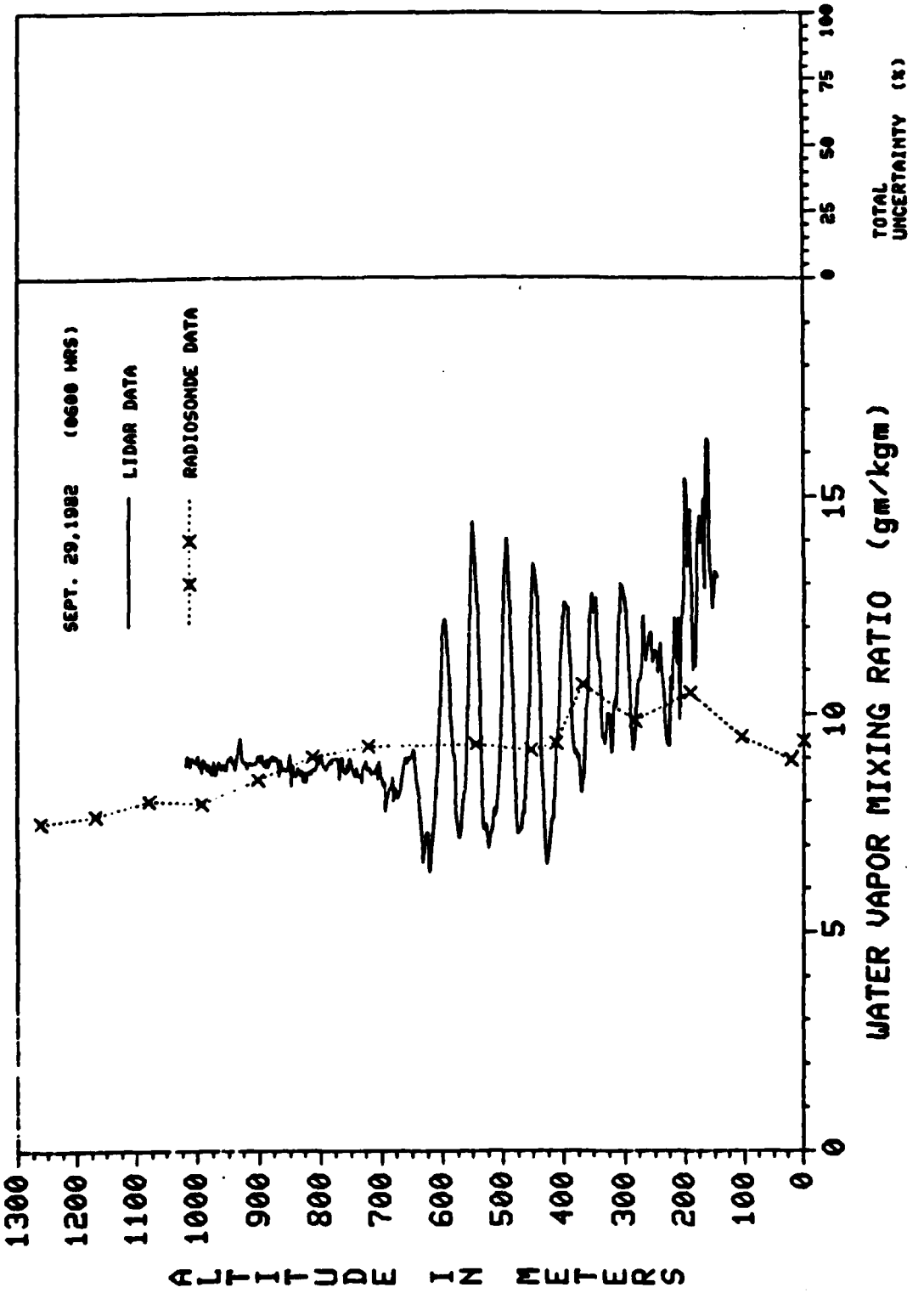

FIGURE 11. HIGH RESOLUTION LIDAR PROFILE

REFERENCES

1. "Variable-Wavelength Solar-Blind Raman Lidar for Remote Measurement of Atmospheric Water Vapor Concentration and Temperature". K. Petri, A. Salik, J. Cooney. Applied Optics, Volume 21, Number 7, 1 April 1982.

2. "An Experimental Solar-Blind Raman Lidar". A. Salik. Phase I Report NADC-80187-30, September, 1980.

3. "Acquisition of Atmospheric Water Vapor Profiles by a Solar-Blind Raman Lidar". J. Cooney, K. Petri, A. Salik. Atmospheric Water Vapor, Academic Press 1980, Editors A. Deepak, T.D. Wilkerson, L.H. Runke.

4. "Measurements of Water Vapor Profiles Using a Solar-Blind Raman Lidar". A. Salik, K. Petri, J. Cooney. Technical Digest of Optical Society of America, January, 1983.

5. "Laser Monitoring of the Atmosphere". Editor E.D. Hinkley. (Springer-Verlag, Berlin 1976).

6. "Efficient Cavity Dumped Dye Laser". R. Morton, M. Mack, I. Itzkan. Applied Optics, Volume 17, Number 20, 15 October 1978.

APPENDIX A

REPORT ON CAVITY DUMP DEVELOPMENT

REPORT ON CAVITY DUMP DEVELOPMENT

This report describes the results to date (August 1982) of the work on the development of the cavity dump equipment which is designed to operate in an intra cavity position in the flashlamp pumped Phase-R laser which has been used for NADC lidar work.

The basic function of the cavity dumper is to provide a means of obtaining short (<30 ns), highly efficient (≈80% normal mode laser operation) laser pulses for use with the NADC lidar.

Earlier efforts at NADC to obtain pulse conversion efficiencies exceeding 20% had been unsuccessful. Whereas the flashlamp pumped Phase-R dye laser would, in the so-called normal mode (≈500 ns pulse duration), provide energies as high as 200 mJ per pulse using Rhodamine 6-G, the cavity dump mode, which gave pulse durations measured at ≈30 ns, failed on the other hand to provide output pulse energies in excess of 20-40 mJ. Since this output had to be frequency-doubled, this resulted in very low, doubled power (≈1.0 mJ or less) and, as a consequence, this provided unacceptable lidar output power/energy.

Initially, it was felt that there were depolarization effects arising inadvertently from some of the components in the laser cavity, which resulted in reduced output. As it turned out, the current experimentation has brought into question the underlying theory of operation. Briefly, the theory is defined in the usual manner by sets of rate equations involving the lasing field (photons) and the lasing levels and loss (triplet states) levels of the lasing material.

It is not so much that the equations themselves are improper as it is the relative importance of the various terms. But this is still somewhat conjectural. Clearly, the theory needs to be examined a bit further. More importantly, however, the various parametric data on say the 6-G dye have to be reexamined.

A series of experiments were begun to see if the specifics of the power conversion efficiency could be denominated. Earlier work (A. Salik) had indicated that the conversion from normal mode to cavity dump mode (inside the laser cavity), achieved basically by replacing a 40% reflecting output flat by a 100% reflecting flat, had succeeded in increasing the internal field (lasing flux) by only a factor of 2-3 instead of the hoped for factor of 10-15. This result indicated the presence of some unaccounted for loss mechanism inside the cavity. The initial guess of some depolarization of the laser field was ruled out early and a straightforward loss inside the cavity was sought.

The various elements in the cavity were examined (by a one-by-one insertion and removal procedure). In addition, a variable iris was inserted in the cavity to obviate wall effects in the dye cuvette.

None of these efforts proved fruitful. A second, much larger Phase-R system (3.0 J/pulse) was also employed in a similar series of experiments. As well as looking for non-linear, large signal gain saturation effects, various model (lasing field) structures were employed and these procedures were equally fruitless.

At the present state of things, certain earlier possible sources of trouble have been eliminated or downgraded. Indeed, the only really strong candidate left for examinations is the dye itself. For example, the triplet losses could be larger than estimated or other parameters could have been poorly estimated, or because of the source or supply, the dye could be contaminated. Triplet quenching was not tried during this series of experiments.

Operationally, the next step would be to back off one step further and to set up a series of experiments on the dye properties themselves. On whether or not this is a worthwhile endeavor, more below.

There is every clear indication up to this point in the work that so long as the solar-blind Raman lidar is the basic remote sensing technology of choice, a tunable uv output spectra is required.

The choice made in 1979 (cavity dumped, flashlamp pumped, doubled dye) has not lived up to manufacturers' claims or our expectations. Existing technology provides an alternative system such as the rare gas halide laser. (KrF)

Currently, while still involved in the proof of principle phase of the work, the fixed wavelength experiment appears the most advantageous choice. At a later date, the easy conversion of the excimer to XeCl (300 nm) could provide a short duration pulse pump laser for a dye, which could then be doubled to the desired frequency.

One final point on current technology is that quite flexible (but not wholly unlimited) tuning is being rapidly developed via the so-called high pressure Raman cell. Field experience may well show that this type of tuning is more than adequate.

In conclusion, as a result of the lab experiments over the last 8.0 months, we have essentially eliminated some causes of poor operation of the cavity dumped doubled dye. Also, as far as I am concerned, it remains an essentially unproven idea (Itzkan's work to the contrary notwithstanding). Nonetheless, we must clearly keep this idea among the list of future possible technological alternatives. As things stand, we appear to be in a good position to temporize for the moment (as long as the KrF produces). In the meantime, sufficient grounds appear to exist to suggest that the ongoing improvements in the other technologies will move along fast enough to provide a satisfactory alternative to the Phase-R cavity dumper when we need it.

John Cooney

APPENDIX B

APPLIED OPTICS REPRINT

Reprinted from APPLIED OPTICS, Vol. 21, page 1212, April 1, 1982

Variable-wavelength solar-blind Raman lidar for remote measurement of atmospheric water-vapor concentration and temperature

Kenneth Petri, Alfred Salik, and John Cooney

System definition and performance calculations are presented for a variable-wavelength solar-blind Raman lidar capable of remotely measuring profiles of atmospheric water-vapor concentration and temperature. A figure of merit is defined which is related to the wavelength dependent SNR. It is shown that the figure of merit for a particular output wavelength depends critically on the instantaneous total ozone overburden as well as the ozone content from the earth's surface up to a maximum measurement altitude. Figures of merit for water-vapor and temperature profile measurements are presented. Best performance output wavelengths are given, and total output energies required to yield preespecified accuracies are computed.

I. Introduction

A need exists to measure remotely atmospheric water-vapor concentration and temperature profiles from the earth's surface to altitudes of a few kilometers during daylight hours as well as at night. The potential of a solar-blind (SB) Raman lidar to meet this need is described.

An SB Raman lidar can be operated in the same fashion as visible Raman lidars.[1,2] For the measurement of water-vapor and temperature profiles, both the vibrational Raman backscatter from water vapor and N_2 and the Raman rotational backscatter from the atmospheric mix of oxygen and nitrogen are monitored. Temperature profile measurements[3] are obtained by monitoring two optical channels separated in frequency from the output radiation by ~50.0 and 120 cm^{-1} and utilizing optical bandwidths of 10.0 and 20.0 cm^{-1}, respectively. Water-vapor profile measurements are acquired using the 3650.0-cm^{-1} Raman line of water. The purpose of operating a Raman lidar in the SB region of the spectrum (230–300 nm) is to reduce the background noise to a level which allows daytime operation.

The presence of the ozone in the atmosphere is responsible for the SB phenomenon. The ozone cross section begins to increase as a function of wavelength at 230 nm, and it reaches a maximum at ~255 nm. It decreases rather rapidly until ~285 nm where the ambient solar flux begins to increase significantly. By 295 nm the SB phenomenon has largely disappeared, although vestiges of the absorption extend to ~325 nm. The presence of atmospheric ozone is advantageous when rejecting background radiation; however, the same absorption process which prevents the incoming solar radiation from reaching the lidar is also responsible for attenuating both the output lidar signal and backscattered return signal as it propagates through the atmosphere. As a consequence the optimal lidar operating wavelength is a function of the instantaneous amount of ozone in the atmosphere.

A figure of merit (FOM) is defined to quantify the net change in the SB lidar SNR that is realized because of the presence of atmospheric ozone. On the one hand, the ozone reduces the solar background noise level 7–8 orders of magnitude; on the other hand, it reduces the lidar signal strength ~3 orders of magnitude. The FOM takes these countervailing features into account and readily permits the identification of the wavelength of maximum SNR for a given ozone condition in the atmosphere. As a concomitant of the definition, the FOM is also a function of the measurement altitude.

II. Theory and Evaluation of the FOM

An FOM is defined which is related to the wavelength dependent SNR. It is defined by considering all the relevant wavelength dependent terms which are involved in the magnitude of the received signals. In the

John Cooney is with Drexel University, Physics & Atmospheric Sciences Department, Philadelphia, Pennsylvania 19104; the other authors are with U.S. Naval Air Development Center, Warminster, Pennsylvania 18974.

Received 13 August 1981.

case of the water-vapor measurement, two received signals are involved. One is the Raman shifted water-vapor wavelength, and the other is the Raman shifted nitrogen wavelength. A water-vapor FOM(Λ) is defined as follows:

$$\text{FOM}(\Lambda) = \frac{T_0(\lambda_0 h_1) T_1(\lambda_1 h_1) T_2(\lambda_2 h_1)}{\lambda_0^4 \alpha_1(\lambda_1) \alpha_2(\lambda_2) + K}, \quad (1)$$

where λ_0 = transmitted wavelength,
h_1 = target height,
λ_1 = received wavelength (water vapor),
λ_2 = received wavelength (nitrogen),
$\alpha_1(\lambda_1)$ = transmittance through the entire atmosphere at λ_1,
$\alpha_2(\lambda_2)$ = transmittance through the entire atmosphere at λ_2,
$T_1(\lambda_1 h_1)$ = transmittance from height h_1 to sensor at λ_1,
$T_2(\lambda_2 h_1)$ = transmittance from height h_1 to sensor at λ_2,
$T_0(\lambda_0 h_1)$ = transmittance to height h_1 at λ_0, and
K = nonwavelength dependent constant.

The FOM(Λ) involves transmission between the lidar and the maximum measurement altitude (a few kilometers) at the three wavelengths and increases as any or all of the transmittances increase. These terms are T_0, T_1, and T_2. Each transmittance term is the sum of contributions from Rayleigh scattering, aerosol, and ozone attenuation. The FOM(Λ) increases as the transmitted wavelength decreases varying as λ_0^{-4}. The wavelength to the fourth power in the denominator is the wavelength dependence of the Raman process. The remaining terms α_1 and α_2 are the transmittances through the entire atmosphere. They are present in the denominator to account for the effect of the ambient daytime flux on the noise level in the receiver channels. K is a wavelength independent constant which is added to limit the value of the denominator because the products (α_1) and (α_2) can become exceedingly small. Ideally, the SB lidar is chosen to operate at wavelengths so that the ambient daytime flux (α_1 and α_2) background noise contribution will add ~1.0% to the existing noise from all other sources at the maximum range. This level eliminates background as a practical problem. Since the limiting source of noise on the signal can be shown to be the shot noise on the received signal, it is possible to compute the magnitude of the noise for a specific set of both atmospheric and system parameters for a given range. However, atmospheric conditions are so variable that it would be necessary to adjust output wavelength from one set of lidar measurements to the next to achieve an optimized condition. This is undesirable from an operational point of view. Therefore, a fixed ambient background level is chosen to fall slightly below the level of 1.0% of the shot noise. It can be seen that the function of K is to establish an upper limit to the value of FOM(Λ) regardless of the values of the products (α_1) and (α_2).

The amount of reduction of ambient solar flux required to make an SB lidar shot noise limited during daytime operation can be determined by considering ordinary day–night visible flux ratios. For the visible (400–700-nm) region of the spectrum, the ambient flux ratio of direct sunlight to nighttime darkness (below mean starlight) at the surface is $\sim 10^{+8}$–10^{+9}. Outside the earth's atmosphere the solar flux ratio in the SB region (230–290 nm) to the visible region is $\sim 10^{-1}$. Since visible-wavelength Raman lidars operating at night are typically shot noise limited, $\sim 10^{+8}$ reduction of ambient solar flux in the SB region is required. These flux ratios are used as the basis for setting the otherwise arbitrary background levels.

It should be noted that it is possible to operate an ordinary Raman lidar in the visible portion of the spectrum (400–700 nm) in the daytime. To do this, however, imposes requirements on the lidar design as severe as in the case of the differential absorption lidar (DIAL), where there is a need for a very narrow optical bandwidth in the receiver channels. Because of this the DIAL system design is constrained to a very small angular field of view. As a consequence, the level of ambient solar flux entering a receiver channel is at a very low level and contributes little to the receiver noise level. However, the price which is paid to incorporate the needed mechanical and thermal stability into such a system is significant. The SB Raman lidar can be built with optical and mechanical stability constraints corresponding only to that of the ordinary lidar. Hence, the exploitation of the SB phenomenon is dictated in considerable part by economic constraints.

Plots of the FOM(Λ) (K set equal to 10^{-18}) are given in Fig. 1 for several values of visibility. Although visibility as such has little meaning for the solar-blind

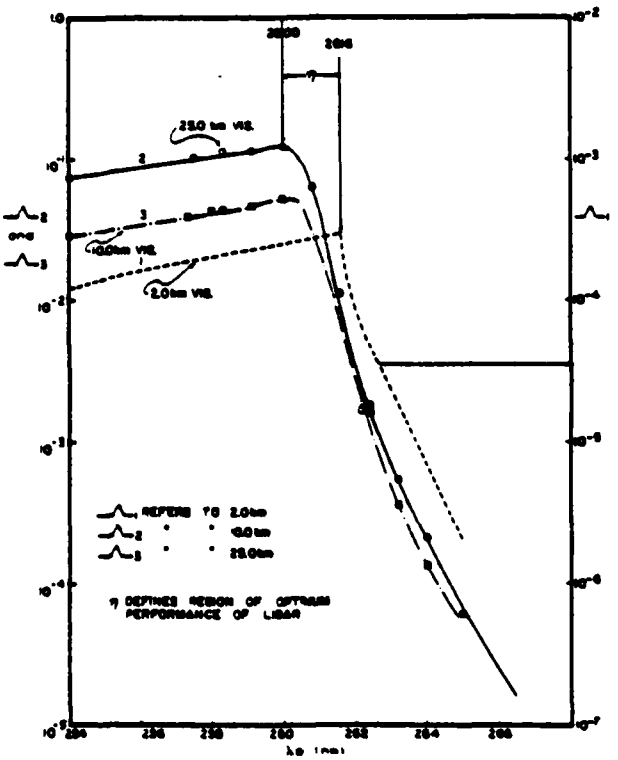

Fig. 1. Figure of merit (H_2O).

wavelength region, it is used here to characterize the aerosol loading of the atmosphere in a way identical with that used in the Elterman[4] attenuation tables. It is seen that although aerosol loading has a marked effect on the absolute value of the SNR, the effect on optimum wavelength η is relatively small.

Similar to the measurement of water vapor, FOM(Ξ) is defined for the measurement of temperature as follows:

$$\text{FOM}(\Xi) = \frac{T_0^2(\lambda_0/\lambda_1)}{\lambda_0^4 \alpha_0^2(\lambda_0) + K}, \tag{2}$$

where $T_0(\lambda_0/\lambda_1)$, λ_0^4, and K are as previously defined, and $\alpha_0(\lambda_0)$ is the transmittance through the entire atmosphere at λ_0.

The definition of the FOM(Ξ) reflects the particular choice of measurement strategy. The Raman rotational spectrum bands of the two received wavelengths to the incident wavelength are so close together on the wavelength axis that variations in the relative transmissions of these three wavelengths are negligible. In the 285-nm spectral region, the three wavelengths span only a 1-nm interval.

The FOM(Ξ) with K equal to 10^{-18} as a function of wavelength λ_0 for various visibility conditions is shown in Fig. 2. In essence the FOM(Ξ) is a function of only the one wavelength. As in the case of the FOM(Λ) the significant changes in visibility due to changes in aerosol loading do not change the optimum wavelength very much. On the contrary, as seen below, modest changes in ozone loading have a more pronounced effect on optimum operating wavelength.

The curves of FOM(Λ) and FOM(Ξ) vs wavelength (Figs. 1 and 2) have been computed using the mean value of the ozone loading because the natural variability of the ozone is difficult to characterize precisely.

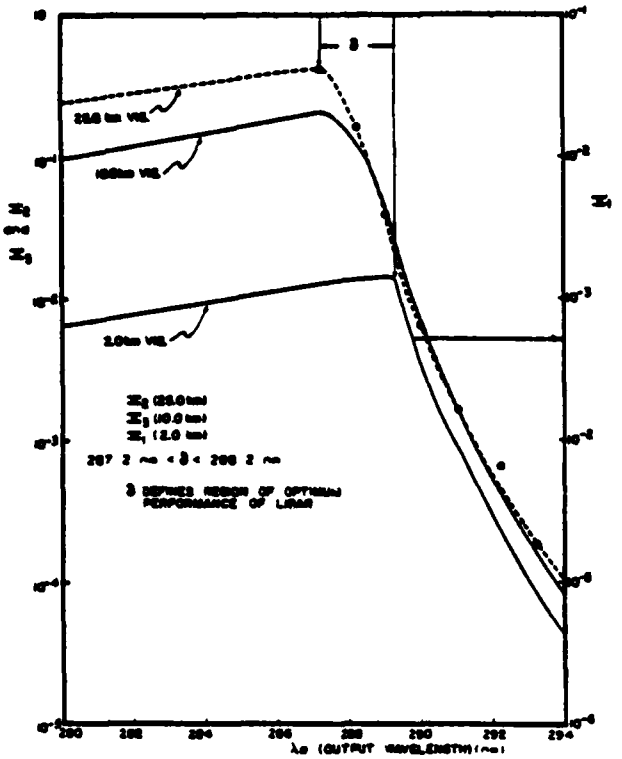

Fig. 2. Figure of merit (temp).

III. Ozone Variability

Atmospheric ozone undergoes significant temporal and spatial changes. The temporal and spatial variability of the amounts of ozone in the atmosphere has a primary effect on SB lidar design. Hence, a survey of these variations is given to establish the magnitude of the problem which is created.

The temporal variability of O_3 is both natural and man-made. The man-made variations have been the subject of intensive study over the past few years. However, aside from the potentially hazardous long-term (decades) anthropogenic changes of the secular variety, the naturally occurring changes are significantly the larger of the two. For example, for a typical mid-latitude station, day-to-day variations in total overburden average 10% in winter and 5% in summer. Year-to-year variations can amount to 25%; man-made variations are of the order of a few percent. Longer term natural variations of decade periods are also thought to exist but are somewhat less pronounced than the yearly variation (CIAP monogram 4, DOT-TST-75-54, Final Report). Also records of O_3 at individual stations are known to vary widely.

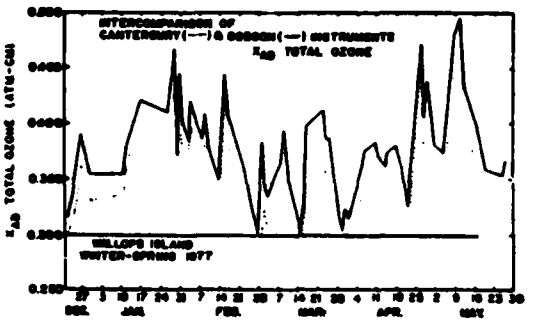

Fig. 3. New Zealand filter Canterbury instrument and the Dobson prism instrument X_{AD} ozone values track well together but with a bias of 7 ± 1.7%. The bias is within the intercomparison calibration uncertainty.

The variation in total overburden measured on a week-to-week basis at Wallops Island, Va. over a 6-month period is shown in Fig. 3. The variation of this weekly average from minimum to maximum is ~70%. Day-to-day minimum to maximum variation, however, is to the lidar user a more significant statistic than average weekly or daily variations. This is because one day is the usual period of a set of measurements.

The intercomparison between the classic Dobson instrument which acquires the value of the ozone overburden as contrasted with a newer but much simpler filter instrument[5] (the so-called Canterbury instrument) is also shown in Fig. 3. The variations in data

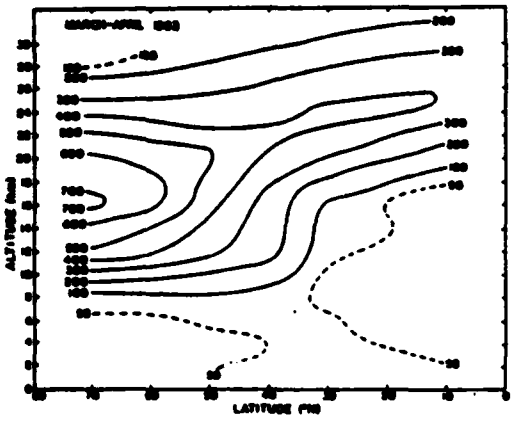

Fig. 4. Average ozone density over the North American continent derived from ozonesonde network data for Mar.–Apr. Values for the contours are $\mu g\ m^{-3}$; divide values by 2.14×10^4 for density in atm cm km^{-1}.

Table I. Surface Comparison Data

DATE	TIME (EDT)	WALLOPS ISLAND DATA (O_3) (ppb)	WALLOPS STATION (O_3) (ppb)
9/9	2200	32.8	27.4
9/10	0200	11.2	25.0
9/10	1100	26.5	32.0
9/10	1600	59.0	58.4
9/11	0200	40.8	46.8
9/11	1100	30.0	35.1
9/11	1600	34.2	46.0
9/11	2200	6.4	30.5
9/12	0200	20.4	19.6
9/12	1100	39.6	38.3

(ppb IS PARTS PER BILLION OF OZONE IN AIR)
SIMULTANEOUS COMPARISON OF GROUND DENSITIES OF O_3 AT POINTS 10 MILES APART

obtained with the two instruments give an appreciation of the relative accuracy of the different methods of obtaining O_3 overburden data.

The data shown in Fig. 3 taken at Wallops Island are a representative sampling of the kinds of variation that are to be expected at a given measurement site. There are also systematic worldwide O_3 variations in both latitude and longitude. Figure 4 shows, for example, the latitude–altitude plot for spring for the northern hemisphere.[6]

The variability of the total atmospheric overburden of O_3 is of sufficient magnitude to cause changes in the FOM and therefore the optimum SB lidar operating wavelength. Even more pronounced, however, is the variability of the O_3 density in the first kilometer. This variation causes changes in the atmospheric transmission of the lidar signals and therefore the optimum operating wavelength.

A sample of the O_3 variation that can occur near the surface is given in Table I.[6] The data of O_3 density given in parts per billion (ppb) are listed for two instruments at two places ~16 km (~10 miles) apart at Wallops Island for Sept. 1977. Thus, as with the O_3 overburden, the O_3 surface density also has significant variability.

Model atmospheres have been developed[5] which characterize the large O_3 changes which occur in the atmosphere due to varying combinations of random and systematic changes. A mid-latitude O_3 model is shown in Table II.[5] The prime quantitative feature of the model is that the total overburden is 0.345 atm cm. This corresponds to 9.27×10^{22} molecules/m^2. The overall variability is 30%. This model is used in the SB lidar system performance calculations to follow.

The O_3 variability in the atmosphere dictates that the SB transmitter/receiver wavelength interval be made variable if maximum lidar efficiency is required.

IV. FOM and Performance Calculations

The relationship between the O_3 density from the surface to the measurement altitude and the total overburden at any given time and place is not well understood. For computational purposes it will be assumed that the overburden and the surface density are completely independent. Thus, there can be a combined maximum overburden with a minimum surface-to-measurement-altitude density and a minimum overburden with a maximum surface-to-measurement-altitude density. In this way, limits of the change in operating wavelength can be determined. This procedure can put rational upper and lower bounds on the expected changes in optimum operating wavelengths as determined by the FOM calculations. FOM(Λ) calculations utilizing the ozone variations described by the Elterman model[4] and the Krueger model are plotted as a function of wavelength in Fig. 5. A 2.2-nm difference in optimum wavelength is predicted. Optimum wavelength determined from FOM(Λ) calculations utilizing the Krueger model is plotted as a function of O_3 overburden in Fig. 6. Computations for FOM(Ξ) can be made in a similar fashion.

For the shot noise limited situation and at the optimum wavelength as determined by mean O_3 conditions, the anticipated uncertainties for the measured quantities have been computed. Uncertainties in the temperature and water-vapor measurements due to shot noise are plotted in Figs. 7 and 8. These curves show what output energy must be used to produce the given uncertainty in the measurements of the water vapor and temperature at 1.0 km. For simplicity, 100-m altitude resolution was used in these calculations.

V. Laser Selection

There are three laser transmitter choices available for the SB lidar: (1) a quadrupled Nd:YAG at 265 nm; (2) a doubled dye with variable wavelength; and (3) an excimer at 248 nm (or possibly 285 nm).

The YAG laser is the most reliable in operation and the excimer the most powerful, but both have fixed

Table II. Mid-Latitude Ozone Model

Geometric Height Z, m	Geopotential Height H, m'	Number Density m^{-3} n_3	Number Density Variability m^{-3} σ	Number Density Percent Variability $100\sigma/n_3$	Column Density atm-cm/km ϵ_3	Mass Density kg/m^3 ρ_3	Partial Pressure mb p_3	Mass Mixing Ratio kg/kg r_3
2000	1999	6.8 (+17)	3.8 (+17)	56	2.5 (-3)	5.4 (-8)	2.6 (-5)	5.4 (-8)
4000	3997	5.8	2.9	50	2.1	4.6	2.1	5.6
6000	5994	5.7	3.0	53	2.1	4.5	1.9	6.8
8000	7990	6.5	5.9	90	2.4	5.2	2.1	9.9
10000	9984	1.13 (+18)	1.23 (+18)	109	4.2	9.0	3.5	2.18 (-7)
12000	11977	2.02	1.58	78	7.5	1.61 (-7)	6.0	5.16
14000	13969	2.35	1.48	63	8.7	1.87	7.0	8.21
16000	15960	2.95	1.42	48	1.10 (-2)	2.35	8.8	1.41 (-6)
18000	17949	4.04	1.23	30	1.50	3.22	1.21 (-4)	2.65
20000	19937	4.77	0.98	21	1.77	3.80	1.43	4.27
22000	21924	4.86	0.82	17	1.81	3.87	1.47	6.0
24000	23910	4.54	0.61	14	1.69	3.62	1.38	7.77
26000	25894	4.03	0.55	14	1.49	3.21	1.24	9.39
28000	27877	3.24	0.45	14	1.20	2.57	1.00	1.02 (-5)
30000	29859	2.52	0.33	13	9.38 (-3)	2.01	7.88 (-5)	1.09
32000	31840	2.03	0.34	17	7.55	1.62	6.40	1.19
34000	33819	1.58	0.27	17	5.88	1.26	5.10	1.27
36000	35797	1.22	0.17	14	4.54	9.72 (-8)	4.03	1.34
38000	37774	8.73 (+17)	1.10 (+17)	13	3.25	6.96	2.95	1.30
40000	39750	6.07	0.79	13	2.26	4.84	2.10	1.21
42000	41724	3.98	0.44	11	1.48	3.17	1.40	1.06
44000	43698	2.74	0.49	18	1.02	2.18	9.89 (-6)	9.67 (-6)
46000	45669	1.69	0.36	21	6.29 (-4)	1.35	6.23	7.86
48000	47640	1.03	0.17	17	3.83	8.20 (-9)	3.85	6.23
50000	49610	6.64 (+16)	1.10 (+16)	17	2.47	5.29	2.48	5.15
52000	51578	3.84	0.7	18	1.43	3.06	1.43	3.8
54000	53545	2.55	0.68	27	9.49 (-5)	2.03	9.28 (-7)	3.18
56000	55511	1.61	0.37	32	6.00	1.28	5.74	2.58
58000	57476	1.12	0.29	26	4.17	8.93 (-10)	3.90	2.25
60000	59439	7.33 (+15)	2.5 (+15)	34	2.73	5.85	2.50	1.88
62000	61401	4.81	1.8	38	1.79	3.83	1.60	1.59
64000	63362	3.17	1.2	38	1.18	2.52	1.03	1.36
66000	65322	1.72	0.66	38	6.4 (-6)	1.37	5.5 (-8)	9.6 (-7)
68000	67280	7.5 (+14)	5.1 (+14)	68	2.8	6.0 (-11)	2.4	5.5
70000	69238	5.4	3.1	57	2.0	4.3	1.6	5.1
72000	71194	2.2	1.7	77	8.2 (-7)	1.8	6.5 (-9)	2.8
74000	73148	1.7	0.9	53	6.3	1.3	4.9	2.9
Total Ozone Amount = 0.345 atm-cm								

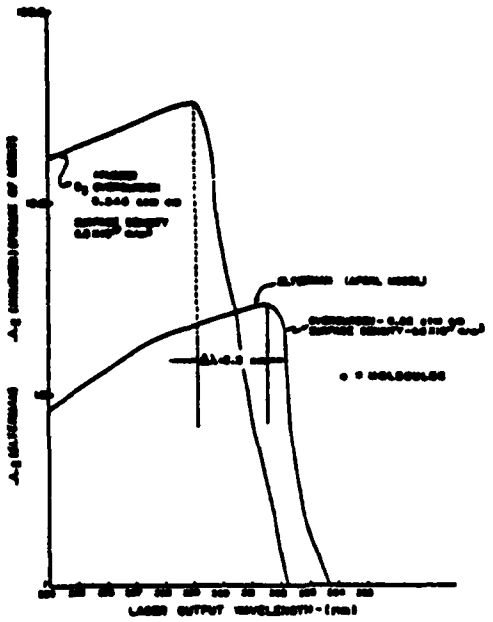

Fig. 5. O_3 plot of figures of merit for optimization of laser output wavelength for water-vapor measurement in which two O_3 models are compared. They are the so-called Krueger (mid-latitude) model and the Elterman (AFCRL) model. The absolute values of the ordinate numbers do not have too much significance, but the relative values are an index of relative performance.

Fig. 6. Plot of optimum operating wavelength of the lidar as judged by maximization of the figure of merit of lidar operation for the measurement of water-vapor profiles (Λ). In turn Λ is maximized by maximizing SNR. It should be emphasized that the calculations are based on a Krueger model O_3 atmosphere, which while clearly satisfactory on an average basis does not take into account that a given atmospheric situation may cause Λ to be optimized outside the wavelength bounds shown.

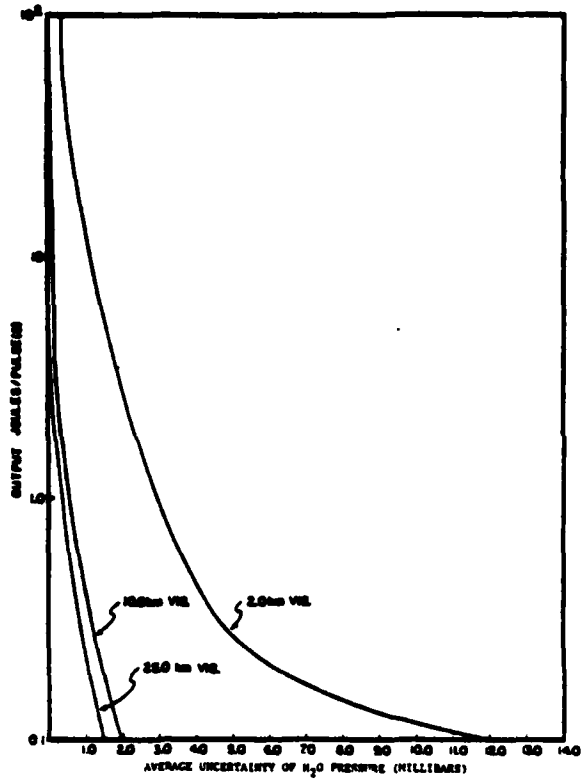

Fig. 7. Uncertainty of H_2O measurement. The statistical uncertainty which arises in the water-vapor measurement as a function of the output lidar energy is shown. The calculations refer to a system with a 0.5-m^2 receiver area and 3.0-MHz receiver bandwidth. The range employed for the calculations is 1.0 km, and the resolution interval is 100 m. The water-vapor cross section used is 2.51×10^{-33} m^2 sr^{-1} at 281.0 nm. The lidar is assumed to be shot noise limited.

wavelength outputs. The FOM calculations show that the Nd:YAG could be used for water-vapor measurements but would be quite unsuited for temperature measurements being so far from the optimum operating wavelength. The bromine excimer (when available) with operation at 285 nm would be preferred because of its larger power which is useful for temperature measurements but would operate for many ozone conditions with a much inferior SNR relative to the dye laser. For water-vapor measurements, the 248-nm excimer could challenge the dye operation because of its large power output. However, handling problems can be very severe with excimer materials. In any event, the current state-of-the-art dye laser need only be equipped with a relatively modest amplifier in the visible to equal the excimer power performance. For many ozone conditions the gain in SNR achieved with a dye system at optimum operating wavelength exceeds the relative power advantage of the excimer. Finally, the relative advantage of the dye laser increases, when operating at its optimum operating wavelength, as the distance or range from the surface to measurement altitude is increased.

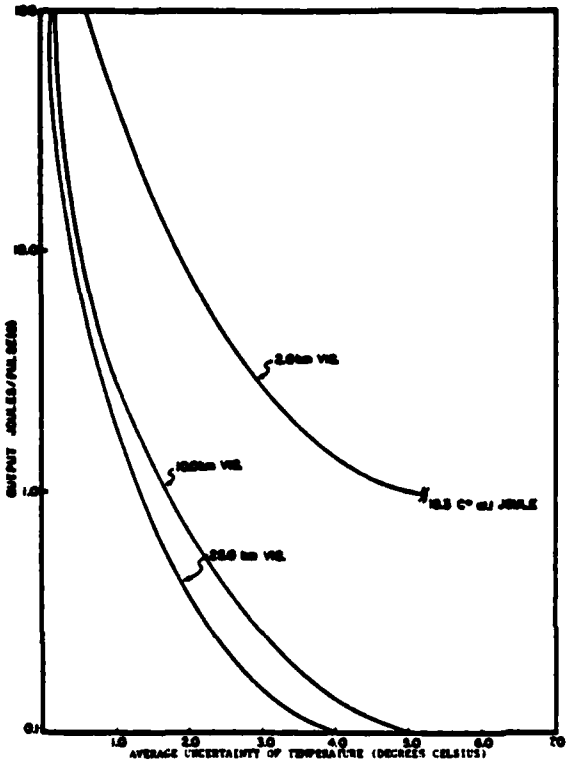

Fig. 8. Statistical uncertainty of temperature measurement. The statistical uncertainty which arises in the water-vapor measurement as a function of the output lidar energy is illustrated. The calculations refer to a system with a 0.5-m^2 receiver area and a 3.0-MHz receiver bandwidth. The range employed for the calculations is 1.0 km, and the resolution interval is 100 m. The O_2 and N_2 Raman rotational cross section is given as 1.36×10^{-32} m^2 sr^{-1} at 286.0 nm. The lidar is assumed to be shot noise limited.

Table III. Increased Power Requirements of Excimer and Quadrupled Nd:YAG Lasers Relative to the Wavelength Optimized Dye Laser [a]

Measurement altitude (km)	Excimer laser (284.5 nm)	Quadrupled Nd:YAG (265 nm)
1	26.5	225.0
2	416.0	237.0
3	4103.0	86.8
4	3.3×10^4	59.0
5	2.2×10^5	45.0

[a] Increased output power requirements at two interesting wavelengths relative to the power output of the wavelength optimized dye laser achieve equal SNR at the receiver. The O_3 overburden used is that shown in Table II. The multiplicative power factor for a laser operating at 248.5-nm (excimer laser) and a laser operating at 265.0 nm (quad/YAG) as compared with that needed for the wavelength optimized dye laser is listed. The atmospheric visibility conditions correspond to a 2.0-km visibility range.

In Table III the increased average power requirements at the fixed excimer and YAG wavelengths relative to a wavelength optimized dye laser are shown. From this one can see the multiplicative power factors by which the YAG and excimer must exceed the dye laser output to achieve equal SNR. It is seen that for values of the O_3 overburden used the dye laser yields significant operational advantages.

It is interesting to quantify in certain appropriate conditions the results of the choice of the tunable dye laser over that of the excimer and quadrupled YAG as the lidar transmitter. It is seen in Table III that at 2.0 km the excimer requires an average power 416.0 times greater than the dye to obtain SNR equal to the dye. The quad/YAG requirement for equal SNR mandates an increase in output power by a factor of 237.0 over the dye. As noted, the meteorological range for these computations is given as 2.0 km. For greater visibility, the O_3 overburden exerts a greater influence relative to the aerosol overburden, and these multiplicative ratios get even greater.

Finally, as seen in Ref. 7 preliminary measurements have already been made employing a quad/YAG system. Although these experiments have given a proof of principle, the projected measurement error could be made to be somewhat smaller. It would appear that the dye laser, because of its tuning characteristics, can enjoy a significant increase in SNR for equivalent output power. As noted in Table III, the factor of 237.0 at 2.0 km could permit an increase in statistical accuracy for equivalent integration time output power and resolution element of a factor slightly in excess of 15.0. This would permit reduction of measurement error to more useful levels.

References

1. J. A. Cooney, J. Appl. Meteorol. 9, 182 (1970).
2. D. A. Leonard, Nature London 216, 142 (1967).
3. J. A. Cooney, J. Appl. Meteorol. 11, 108 (1971).
4. L. Elterman, Environmental Research Paper 285 (Air Force Cambridge Research Laboratories, Bedford, Mass., Apr. 1968).
5. A. J. Krueger and R. A. Minzner, J. Geophys. Res. 81, 4477 (1976).
6. R. E. Basher, NASA Tech. Paper 1277, Wallops Island, Md. (1978).
7. D. Renaut, J. C. Pourny, and R. Capitini, Opt. Lett. 5, 233 (1980).

APPENDIX C

ATMOSPHERIC TEMPERATURE PROFILES

NAVAL AIR DEVELOPMENT CENTER

WARMINSTER, PENNSYLVANIA 18974

3012

18 Mar 1983

ATMOSPHERIC TEMPERATURE PROFILES

This is a Technical Memorandum on Design considerations for the receiver sub-components of the NAVAIRDEVCEN Lidar necessary for the acquisition of atmospheric temperature profiles.

J. Cooney

The Boltzmann equilibrium distribution of energy across the pure rotational Raman spectrum (RRS) of the atmospheric mix of nitrogen and oxygen provides a means for the acquisition of atmospheric temperature profiles with the NAVAIRDEVCEN solar blind Raman lidar. Because the state occupation numbers of this spectrum are determined to a very high level of accuracy by this thermal distribution, a means exists of acquiring very accurate (≈ 1.0 deg. K) temperature data from measurement of the relative intensities of prescribed portions of this spectral band.

In the vicinity of 248.5 nm output exciting radiation of the lidar, the pure RRS is a band of lines in the close vicinity of the exciting line ($\Delta F_{max} \approx 20.0\ cm^{-1}$). The RRS is roughly equally spaced and is of approximately equal measure on both sides of the exciting line on the wavelength axis.

By interposing very narrow band (FWHM ≈ 5.0 cm^{-1}) spectral filtering in two selected portions of this spectrum, a ratio of the received intensities of the two portions from a given altitude interval can be formed which provides a measure of the atmospheric temperature from that altitude interval.

The receiver sub-component of the lidar consists of two (or more) receiver channels through each of which a narrow portion of the RRS is allowed to pass. The central problem of the design consists in providing filtering in this portion of the UV spectrum which has the moderately narrow bandwidth cited above and in addition provides for very significant rejection in the Raman channel of the so-called Rayleigh or elastic backscatter simultaneously with the acceptance of the appropriate portion of the RRS.

The basic lidar system consists of a transmitter (excimer laser purchased from Tachisto Inc., operating at 248.5 nm) which provides a 0.75 joule pulse of radiation in 20 nsec. This transmitter is co-mounted on an optical telescope comprising a 30.0 in. diameter primary with the electro-optical receiver sub-component. The basic output pulse from the laser provides a continous flow of backscatter radiation from the atmosphere. This signal is acquired by the telescope and thence directed into the electro-optical receiver sub-component. The basic function of the receiver is to select those prescribed portions of the RRS spectrum while adequately rejecting the remainder. Having obtained the wanted portion of the optical spectrum, the attendant photomultipliers strip the r.f. signal from the optical carrier and so provide the raw data needed for temperature profiles.

In order to achieve the ultimate goal of the temperature profile, present plans call for the modification of the existing lidar at NAVAIRDEVCEN currently being employed to acquire humidity profiles of the atmosphere. Because of this there is, in addition to the receiver sub-component design cited above, two other major redesign problems. Thus, the current laser needs to be modified to put out radiation with a 0.1 nm bandwidth (or less) and, in addition, a software package needs to be designed to handle the new data processing requirements. These later two requirements, although expensive in hardware costs and time, are otherwise routine. In fact, an intermediate though not a definitive solution of the laser problem consists in replacing the current cavity optics with unstable resonator optics and a ruggedized grating. A more useful though expensive procedure is to proceed to an injection lock (so-called oscillator-amplifier) system.

Before proceeding with the center piece subject (design of the interferometer), it is useful to discuss the background spectroscopic theory and deal with the measurement strategy and software. The RRS from a sample is, as noted above, a series of lines. The strength of the scattered intensity from the sample I_j is given as

$$I_j = I_o\ (245)\ g_j N(\nu_o \pm \nu_{ROT})^4\ \frac{3(J+1)\ (J+2)\ (2j+1)\ \gamma_o^2}{2(2J+3)\ (2J+1)\ Z} \exp\left[-\frac{J(J+1)\ hcB}{kT}\right]$$

I_o = incident intensity falling on sample

g_j = nuclear degenercy factor for line J = g(J)

N = number density of scatterers

ν_o = exciting frequency

ν_{ROT} = amount of frequency shift from exciting line = $4B(J+\frac{3}{2})$

J = rotational quantum number

$Z = \frac{kT}{hcB}$

B = rotational constant $(\frac{h}{8\pi^2 cI})$

I = molecular moment of inertia

h = Planck's constant

T = temperature of sample

γ_o = Anisotropic part of scattering tensor

In more convenient terms

$I_j = I_o \xi = I_o N \sigma$ Let $\xi_j = \xi(J)$

ξ_j = Raman rotational volumetric scatter from line J

σ_j = Raman rotational cross section per molecule at J

N = Number density of scatterers

In the actual experimental arrangement employed, two Raman channels are provided for in the lidar receiver. Each individual signal, $P_1(\lambda_1)$ and $P_2(\lambda_2)$, is monitored and the two signals which are functions of range are acquired and stored. In order to understand how the temperature profile is obtained, note that P_1 and P_2 are acquired as radar like signals. Thus

$$P_1(J_1) = \frac{P_o B'(J_1)\ (C\tau/2)\ \xi(J_1)\ T_o\ T(J_1)\ A}{4\pi r^2}$$

$$P_2(J_2) = \frac{P_o B'(J_2)\ (C\tau/2)\ \xi(J_2)\ T_o T(J_2)\ A}{4\pi r^2}$$

$$\frac{P_1(J_1)}{P_2(J_1)} = P(J_1, J_2) = \frac{B'(J_1)\ \xi\ (J_1)\ T\ (J_1)}{B'(J_2)\ \xi\ (J_2)\ T\ (J_2)}$$

T_o = transmission to altitude r at exciting (laser) wavelength

$B'(J_1)$ = the system (channel) electro-optical response in small interval of wavelength λ_1. Ditto $B'(J_2)$ where the J_1 line occurs at λ_1

$T(J_1)$ = the atmospheric transmission at λ_1 ($\lambda_1 \rightarrow J_1$) from an attitude r to the receiver. Ditto $T(J_2)$

Since $T(J_1)/T(J_2)$ is the ratio of transmissions at wavelengths λ_1 and λ_2 where λ_1 and λ_2 are separated by the order of 0.1 nm, this ratio is set equal to unity. The ratio of $B'(J_1)/B'(J_2)$ is that of the relative response of the lidar for incoming radiation at λ_1 and λ_2 and as such is an instrumental constant and must be determined by some form of calibration (on this, more below). Aside from the ratio of $B^1(J_1)/B^1(J_2)$, the measured ratio P is given as,

$$P = \frac{g(J_1)\ [\nu_o \pm \nu_{rot}(J_1)]^4\ \frac{(J_1+1)\ (J_1+2)}{(2J_1+3)}\ \exp[-J_1(J_1+1)\alpha]}{g(J_2)\ [\nu_o + \nu_{rot}(J_2)^4\ \frac{(J_2+1)\ (J_2+2)}{(J_2+3)}\ \exp[-(J_2(J_2+1)\alpha]}$$

where,

$\alpha = 1/Z$ and

$g(J_1)/g(J_2)$ is a theoretical fixed constant of order unity; $\frac{g(J_1=8)}{g(J_2=12)} = 1.0$

Now $\left(\frac{\nu_o \pm \nu_{rot}(J_1)}{\nu_o \pm \nu_{rot}(J_2)}\right)^4 = .9964$ and

$$\frac{(J_1+1)\ (J_1+2)/(2J_1+3)}{(J_2+1)\ (J_2+2)/(2J_2+3)} = .7$$

Hence $P(J_1 = 8,\ J_2 = 12) = .7\ \left[\frac{\exp\ (-203.76/T)}{\exp\ (-441.5/T)}\right]$

which, for T=300 becomes P=1.546

Parenthetically it should be noted that there are two tables appendaged to this report. One table provides accurate values of line assignments and the second table provides values of the relative strength of the line intensities. This can serve as a ready reference for the interested reader.

In general $260 \leq T \leq 300$ deg. K. The ratio P will generally be in the neighborhood of unity. The lack of the precise knowledge of the instrumental constants comprising a part of the calculated value of P (e.g., B(J)) can be overcome by a measured value of P backscattered from a region of known temperature.

A prearranged table of calculated values of P for given temperatures can thus be normalized by the measured value for a given temperature and so a temperature profile can be constructed.

As suggested above, the critical design consideration focuses on the optical filtering required. Because of the very narrow passband needed and also because of the very high rejection ratio of the filtering response I(248.1 nm)/ I(248.5 nm) demanded by the individual Raman channels, the Fabry-Perot interferometer is the technology of choice. Before getting into the design calculations which require certain input design specifications, an examination of the relevant cross sections involved will indicate the magnitude of these input parameters.

To begin with, the absolute value of a cross section from which all other absolute values are to be derived, must be cited. Schrotter (Univ. of Munich) has compiled a list of the best measurements of the absolute value of the cross section of the Q-vibrational of $N_{14}N_{14}$. This is

$$\sigma(\text{Q branch vib})N_2 = 5.05 \pm 0.001 \times 10^{-48} \ (\nu_o - 2331)^4 \ \text{cm}^6 \ \text{str}^{-1}$$

("Raman Spectroscopy" - Springer-Verlag 1979)

Hence

$$\sigma(Q\text{-}N_2)\Big|_{488\ \text{nm}} = 5.49 \times 10^{-31} \text{cm}^2 \ \text{Str}^{-1} \rightarrow 6.9 \times 10^{-30} \ \text{cm}^2$$

In addition, the Rayleigh cross section is given as

$$\sigma(\text{RAY})\Big|_{488\ \text{cm}} = (5.11 \times 10^{-27} - 1.0 \times 10^{-26}) \text{ depending on amount of variable } H_2O$$

For average choose $\sigma(\text{RAY})\Big|_{488\text{ cm}} = 7.5 \times 10^{-27}\ \text{cm}^2$

Using dipole wavelength scaling (i.e., scale by $1/\lambda_4$)

$$\sigma(Q\text{-}N_2)\Big|_{248.5} = 1.02\text{x}10^{-28}\ \text{cm}^2$$

$$\sigma(\text{RAY})\Big|_{248.5} = 1.11\text{x}10^{-25}\ \text{cm}^2$$

σ(Raman Rotational Peak Line) = σ(RRPL)

(J=6) σ (RRPL) $\Big|_{248.5} = (1.9)\ (1.02\text{x}10^{-28}) = 1.94\text{x}10^{-28}\ \text{cm}^2$ (Porto, Appl. OPT.)

(J=8) σ (RRPL) $\Big|_{248.5} = 1.86\text{x}10^{-28}\ \text{cm}^2$ Stokes only

(J=12) σ (RRPL) $\Big|_{248.5} = 1.195\text{x}10^{-28}\ \text{cm}^2$ Stokes only

(J=8) σ (RRPL) $\Big|_{248.5} = 1.466\text{x}10^{-28}\ \text{cm}^2$ anti-Stokes only

(J=12) σ (RRPL) $\Big|_{248.5} = 1.017439\text{x}10^{-28}\ \text{cm}^2$ anti-Stokes only

(J=8) σ' (RRPL) $\Big| = 3.326\text{x}10^{-28}\ \text{cm}^2$ Both stokes and anti-stokes

$$(J\text{-}12)\ \sigma'(RRPL)\Big|_{248.5} = 2.213\times10^{-28}\ cm^2$$ Both stokes and anti-stokes

[σ(RRPL) all for T = 295 deg. K]

$$\frac{\sigma'(RRPL)\ (J=8)}{\sigma(RAY)}\Big|_{248.5} = \frac{3.326\times10^{-28}}{1.11\times10^{-25}} = 2.996\times10^{-3}$$

A factor of 334.

$$\frac{\sigma'(RRPL)\ (J=12)}{\sigma(RAY)}\Big|_{248.5} = \frac{2.213\times10^{-28}}{1.11\times10^{-25}} = 1.99\times10^{-3}$$

A factor of 502.

Hence, photon for photon, there will be 334 times greater Rayleigh signal (J=8) and 502 times greater Rayleigh signal than Raman rotational (J=12) in the backscatter radiation. Allowances must be made for small (a few percent) changes of these numbers due to the slightly different numbers for oxygen. Allowing for the fact that there should be about a 1.0% intrusion of the Rayleigh signal into the Raman channel, a rejection ratio of 5.0×10^4 (RAY/Raman) should be designed into the optical filtering system.

Two final points should be noted concerning the magnitude of the intrusion. Firstly, unlike the near IR, the Rayleigh backscatter, as opposed to the aerosol backscatter, is the more important in the UV. Secondly, the Rayleigh intrusion in both channels is a systematic noise source, not a random noise source. Unlike a random noise source, a ratio will reduce the influence of these systematic intrusions. Thus, consider

$$\frac{A + \varepsilon_1^1}{B + \varepsilon_2^1} = \frac{A}{B}\frac{(1+\varepsilon_1)}{(1+\varepsilon_2)} \quad \text{where } \varepsilon_1 = \frac{\varepsilon_1^1}{A} << 1.0$$

$$\text{and } \varepsilon_2 = \frac{\varepsilon_2^1}{B} << 1.0$$

Given that the ε^1 's represents the Rayleigh intrusions,

$$\frac{A + \varepsilon_1^1}{B + \varepsilon_2^1} \simeq \frac{A}{B}(1+\varepsilon_1)(1-\varepsilon_2) = 1 + (\varepsilon_1 - \varepsilon_2) + \varepsilon_1\varepsilon_2$$

Here, A/B represents the Raman ratio and if $\varepsilon_1 \simeq \varepsilon_2$ only the square of the normalized intrusion signal will be noted. Thus $\frac{A + \varepsilon_1^1}{B + \varepsilon_2^1} \simeq \frac{A}{B}(1 + \varepsilon_1^2)$. It is clearly in the interest of accuracy of the temperature profiles to try to keep $\varepsilon_1^1 = \varepsilon_2^1$. Also, it is no wonder that reduced rejection ratios in a given channel have less of an effect on the accuracy of the measured ratio than might otherwise be supposed. Despite all of the above, as a matter of simple prudence, a third channel designed to measure the Rayleigh or elastic component of the backscatter will be provided for. If needed, such measurements can help further reduce the consequences of the Rayleigh intrusion on the Raman channels.

There are two input design criteria to be considered for the fabrication of the Fabry-Perot interferometric (FPI) optical filtering. Firstly, there is the free spectral range (FSR). This is basically set by the actual wavelength

separation between the maximum Raman rotational signal (J=8) and Rayleigh signal and, in addition, there is the contrast required which is the ratio of the intensities of these two signals.

As a basic design consideration, it is imagined that for a given Raman channel, two FPI's operate in tandem. Commercial 3-pass systems were rejected because large apertures (≈ 1.0 in. dia.) were needed. To begin with, let the total contrast $C = 5.0 \times 10^4$ where $C = C_1^2$ and C_1 is the contrast of the individual FPI. Here, $C_1 = 224.0$. In general $C_1 = \frac{4F_1^2}{\pi^2}$ so $F_1 = 23.44$ (Finesse)

Now also the FSR (J=8) = 151.2 cm^{-1}. This implies a FWHM for the passband of $\Delta W = \frac{151.2}{23.44} = 6.45\ cm^{-1}$. The equivalent wavelength of FWHM, at $\lambda_o = 248.5$ nm equals $\alpha W\ (\lambda) = \frac{6.451}{151.2}(9.36) = 0.03993$ nm ≈ 0.04 nm. The finesse (F) of the pair is given by $F_P = \frac{F_1}{(2^{1/P} - 1)} = \frac{23.44}{(2^{1/2} - 1)^{1/2}} = 36.4$ with P =2.0

This has the consequence of lowering ΔW. Hence the FWHM of the FPI pair = 0.026 nm. This could have the effect of reducing the total transmission of a wideband backscatter signal (e.g., WW = 0.1 nm) by about 35%. It is more instructive to consider a more elaborate calculation to determine such transmission, but first consider the feasibility of obtaining a single finesse $F_1 = 23.44$.

$$\frac{1}{F_1^2} = \frac{1}{F_R^2} + \frac{1}{F_F^2} + \frac{1}{F_P^2} \; ; \; F_R = \frac{\pi\sqrt{R}}{1-R}$$

$$F_F = \frac{M}{2} \; ; \; F_P = \frac{4\lambda L^2}{D^2 d}$$

with

R = plate reflectivity equal to .94

M = flatness spec (m = 100 for λ = 250 nm)

λ = wavelength (2.485×10^{-7} m)

L = focal length (24.4 cm = .254m)

D = aperature (.25" = 6.35 mm = 6.35×10^{-3} m)

d = plate spacing (33.0×10^{-6} m)

F_R (R =.94) = 51.0; F_F ($\lambda/200$) = 50.0

$$F_p = \frac{(4.0)\ (2.485)\ (.25)^2\ (10^{-7})}{(6.35)^2\ (10^{-6})\ (33.0 \times 10^{-6})} = \frac{.62 \times 10^{-7}}{1.33 \times 10^{-9}} = 47.0$$

F_p (D = 5.0 mm) = 76.0

However, F_p exists only for the second FPI. The F_p of the first interferometer is essentially infinite as L approaches infinity. The F_1 = 32.3 for the above conditions. This implies that these parameters, required for F_1 = 23.44, can be realized with modest effort. The most useful parameters to relax are the pinhole aperature and the reflectivity. The design of the second pair of interferometers for the other Raman channel follows the same logic. FSR^1(J=12) = 214.65 cm^{-1} assuming the same contrast as with the first pair F_1^1 = 23.44. Thus ΔW = 9.16 cm^{-1}. $\alpha W(\lambda) = \frac{9.16}{214.65}$ = .0564 nm FWHM.

Also, the combined throughput of each system (transmission maximum) can be given as

$$t_1 = \left(1 - \frac{A}{1-R}\right)^2 \qquad \text{typically } A = .002$$

$$\therefore t_1 = \left(1 - \frac{.002}{1-.94}\right)^2 = .967$$

So $(t_1)^2 = .934$. This peak transmission holds for both channels.

Finally, in order to obtain some appreciation of the net transmission from a given FPI mode, one must integrate the transmission function over the passband interval. The transmission is described in terms of Airy functions. For simplification of analysis this function is typically replaced by a Gaussian function. The transmission passband of the FPI will be represented by the function

$$G_1 = G_{01} \exp\left[- \frac{[(\lambda-\lambda_{c1})^2]}{(\Delta\lambda_1)^2} \right]$$

where G_{01} is the maximum value of transmission at a center wavelength λ_{c1}. The passband halfwidth is $\Delta\lambda_1$. Now it is of interest to determine whether or not it will prove more effective in the presence of a broadband laser output ($\Delta\lambda^1 \approx .1$ nm) to separate the center frequencies of the tandem FPI one with respect to the other. Assuming the Raman line has a typical line width $\Delta\lambda \leq .01$ nm and using a laser output bandwidth of 0.1 nm, the Raman backscatter return from a given line will likewise span about 0.1 nm. It is of interest to determine if the net transmission through the FPI pair will be greater when the center wavelengths are set to different values. Thus consider the integral

$$A = \int_{U_1}^{U_2} G_1(\lambda,\lambda_{c1},\Delta\lambda_1)G_2(\lambda,\lambda_{c2},\Delta\lambda_2)d\lambda = \int_{U_1}^{U_2} G^1 \, d\lambda$$

where

$$G^1 = G_{o1} \exp\left[-\frac{(\lambda-\lambda_{c1})^2}{(\Delta\lambda_1)^2}\right] G_{o2} \exp\left[-\frac{(\lambda-\lambda_{c2})^2}{(\Delta\lambda_2)^2}\right]$$

Initially, consider first the case $G_{01} = G_{02} = G_0$; $\lambda_{c1} = \lambda_c$ and $(\Delta\lambda_1) = (\Delta\lambda)$. Also let $U_1 = -00$ and $U_2 = +00$. Hence Consider the integal

$$A^1 = \int_{-\infty}^{\infty} G_0^2 \exp\left[\frac{-(\lambda-\lambda_c)^2}{(\Delta\lambda)^2/2}\right] d\lambda = \left(\frac{\pi}{2}\right)^{1/2} \Delta\lambda G_0^2 = .5 \text{ for } G_o = 1.0 \text{ and}$$

for $\Delta\lambda = .4$. Next, consider how this result is modified for the orginal limits U_1 and U_2, where $U_2 - U_1 = 0.1$ nm. Consider

$$A^{11} = \int_{U_1}^{U_2} G_0^2 \operatorname{Exp}\left[\frac{-(\lambda-\lambda_c)^2}{(\Delta\lambda)^{2/2}}\right] d\lambda = \int_{-c}^{c} \exp(-\alpha X^2) dx$$

$$= \left(\frac{\pi}{2}\right)^{1/2} \operatorname{erf}(C\alpha^{1/2}) \qquad \text{for } \alpha = \frac{2}{(\Delta\lambda)^2} \qquad \text{and } c = .5$$

$A^{11} = (.5)\operatorname{erf}(1.767) = .494$. Note that the extreme narrowing of the limits of integration has a negligible effect upon the net transmission. This will be so until the limits begin to encroach upon the half power points.

Finally, consider the integral A under the circumstances where the center wavelengths are shifted slightly with respect to one another. Thus,

let $U_1 \leq \lambda_{c1} \leq \lambda_{C_2} \leq U_2$ where $\lambda_{c1} - \lambda_{c2} = -\varepsilon$. Pictorially, for λ_{c1} set at the middle of the band encompassing the disposition of $\lambda_c 2$ within the band U_1 and U_2. This situation is here displayed:

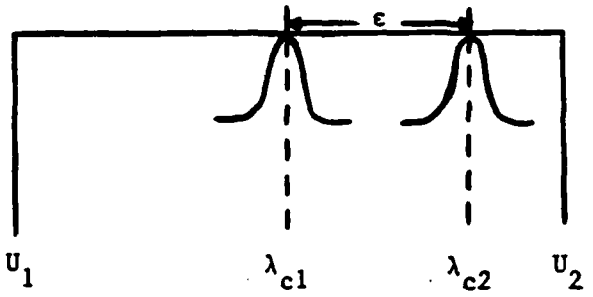

$$\lambda_{c2} - \lambda_{c1} = \varepsilon$$

$$\lambda_{c1} = \frac{U_1 + U_2}{2}$$

for $X = \lambda - \lambda_{c1}$, one can rewrite A as

$$A = \int_{-c}^{c} \exp\left[\left[-\frac{X^2 + (X+\varepsilon)^2}{(\Delta\lambda)^2} \right] \right] dx = \int_{-c}^{c} G^{11}\, dx$$

$$c = U_2 - \lambda_{c1} = +.5$$

$$-c = U_1 - \lambda_{c1} = -.5$$

$$U_2 - U_1 = 1.0$$

$$\lambda_2 = \lambda_{c1} + \varepsilon$$

$$G^{11} = G_o^2 \exp\left[-\frac{X^2 + X^2 + 2X\varepsilon + \varepsilon^2}{(\Delta\lambda)^2} \right]$$

Now, $$\int_U^\infty \exp\left[-\frac{X^2}{4B} - \gamma X\right] dX$$

$$= (\pi B)^2 \left[\exp(B\gamma^2)\right]\left[1 - \Phi\left(\gamma B + \frac{U}{2B^{\frac{1}{2}}}\right)\right]$$

where $$\Phi(y) = \operatorname{erf}(y) = \frac{2}{\pi^{\frac{1}{2}}} \int_o^Y \exp(-t^2)\, dt$$

and where real B > 0 and U > 0. Since -C < 0 there is a need to shift regions of interest to a completely positive region. i.e. redefine $\lambda = \lambda - \lambda_c + 1$ so

$$\int_{U_1^1}^{U_2^1} = \int_{U_1^1}^{\infty} - \int_{U_1^1}^{\infty} = (\pi B)^{\frac{1}{2}} \exp(B\gamma^2) \left[\Phi\left(\gamma B + \frac{U_2^1}{2B^{\frac{1}{2}}}\right) - \Phi\left(\gamma B + \frac{U_2^1}{2B^{\frac{1}{2}}}\right)\right]$$

$$U_1^1 = +1.5$$

$$U_1^1 = +.5$$

Now G^{11} becomes

$$G^{11} = G_o^2 \exp\left[-1 \frac{2X^2+(2\varepsilon-3)X+\varepsilon^2+2}{(\Delta X)^2}\right]$$

$$\therefore \int_{+5}^{1.5} G_o^2 \exp\left[-1 \frac{2X^2+(2\varepsilon-3)X+\varepsilon^2+2}{(\Delta X)^2}\right] dx$$

$$= G_o^2 \exp\left[-\frac{\varepsilon^2+2}{(\Delta X)^2}\right] \left[\left(\frac{\pi}{}\right)^{\frac{1}{2}}(\Delta x) \exp\left(\frac{(3-2\varepsilon)^2}{8(\Delta\lambda)^2}\right) \Phi\left(\frac{\varepsilon}{4} + \frac{1.5 \quad\quad 0}{2(\Delta\lambda)(\pi/8)^{\frac{1}{2}}}\right) - \Phi\left(\frac{\varepsilon}{4} + \frac{.5 \quad\quad}{2(\Delta\lambda)(\pi/8)^{\frac{1}{2}}}\right)\right]$$

It is obvious that this function is a maximum for $\varepsilon = 0$. This implies that displacing the center wavelength of the tandem FPI will only lower the net transmission. Hence both FPI's in the tandem arrangement should be tuned to the same center wavelength.

As a final comment it should be pointed out that despite the favorable outlook provided by this analysis, the important question of signal/noise and upper range limitations have yet to be fully explored.

Initially, working with this interferometer receiver will require a great deal of skill from the experimenter and meticulous care must be exercised during a measurement episode to see that all calibrations and adjustments are punctiliously carried out. This implies not only great care on the part of the experimenter, but requires deletion of the existing 7912 to be replaced by 7612. This is a must.

Also, it should be restated that a third channel needed to acquire the elastic signal must be added to assist in the proper assessment of the effect of the Rayleigh intrusion as a matter of simple design procedure.

Again, there are many things that can serve to diminish the accuracy of these measurements below acceptable values, so please understand that for the first year or so, this is a "hairy" measurement. On the other hand, there is now in the literature documented cases of success so that the goal is known to be achievable.

LINE ASSIGNMENTS

J	$\Delta\nu(N_2)$ cm^{-1}	$\Delta\nu(O_2)$ cm^{-1}	N_2 Å Stokes Lines	O_2 Å Stokes lines	N_2 Å Anti Stokes	O_2 Å Anti Stokes
1	19.894		2486.2		2483.77	
2	27.850		2486.7		2483.28	
3	35.808	25.877	2487.2	2486.59	2482.79	2483.40
4	43.762		2487.7		2482.30	
5	51.715	37.369	2488.2	2487.30	2481.81	2482.69
6	59.667		2488.7		2481.32	
7	67.616	48.855	2489.2	2488.02	2480.83	248198
8	75.563		2489.7		2480.34	
9	83.508	60.337	2490. 6	2488.73	2479.85	2481.27
10	91.450		2490.66		2479.36	
11	99.389	71.809	2491.15	2489.44	2478.87	2480.57
12	107.325		2491.64		2478.39	
13	115.257	83.267	2492.13	2490.15	2477.90	2479.86
14	123.186		2492.63		2477.41	
15	131.110	94.712	2493.12	2490.86	2476.92	2479.16
16	139.265		2493.62		2976.42	
17	147.723	106.143	2494.15	2491.37	2475.91	2478.46
18	154.856		2494.59		2475.47	
19	163.139	117.554	2495.11	2492.28	2474.96	2477.76
20	171.097		2495.61		2474.47	
21	179.056	178.949	2496.10	2492.98	2473.99	2477.06
22	187.013		2496.60		2473.50	
23	194.971	140.893	2497.09	2497.73	2473.01	2476.32
24	202.929		2497.59		2472.53	
25	210.887	152.394	2498.10	2494.44	2472.04	2475.62

λ_o = 2485.Å → 40241.5 cm^{-1}; $B(O_2)$ = 1.427682 cm^{-1}; $B(N_2)$ = 1.98950 cm^{-1}

$\Delta\nu$ = 4B(J+3/2) .44869

Relative Line Strength of N_2 and O_2 Raman Rotational Spectrum

J	N_2 Stokes	N_2 Anti Stokes	O_2 Stokes	O_2 Anti Stokes
0	2.000	0.0		
1	1.76636	0.0	1.77561	
2	4.85986	1.88994		
3	2.97658	0.892971	3.07131	0.921392
4	6.77505	4.25861		
5	3.65168	2.51173	3.94921	2.71638
6	7.53617	5.50532		
7	3.74586	2.85742	4.33561	3.30730
8	7.20507	5.67867		
9	3.36163	2.71807	4.25208	3.43804
10	6.07464	5.03454		
11	2.69461	2.26195	3.80337	3.19270
12	4.64221	3.95243		
13	1.95114	1.68133	3.13804	2.70410
14	3.20361	2.78929		
15	1.28502	1.12895	2.40460	2.11256
16	2.015746	1.78497		
17	0.773188	0.689471	1.71894	1.53282
18	1.16073	1.04151		
19	0.426341	0.384694	1.14986	1.03754
20	0.613225	0.556156		
21	0.215927	0.196713	0.721370	0.657181
22	0.297833	0.272462		
23	0.100598	0.092379	0.425113	0.390379
24	0.133174	0.122720		
25	0.043173	0.039912	0.235634	0.217837

END

FILMED

3-84

DTIC